12-2023

Constraining Silicate Weathering During the Middle Eocene Climatic Optimum (MECO) Using Radiolarian Ge/Si

Olivia R. Laub
Utah State University, ollie.laub@usu.edu

CONSTRAINING SILICATE WEATHERING DURING THE MIDDLE EOCENE CLIMATIC OPTIMUM (MECO) USING RADIOLARIAN Ge/Si

by

Olivia R. Laub

A thesis submitted in partial fulfillment
of the requirements for the degree

of

MASTER OF SCIENCE

in

Geosciences

Approved:

Donald E. Penman, Ph.D. Major Professor	Carol M. Dehler, Ph.D. Committee Member
Tammy M. Rittenour, Ph.D. Committee Member	D. Richard Cutler, Ph.D. Vice Provost of Graduate Studies

UTAH STATE UNIVERSITY
Logan, Utah

2023

ABSTRACT

Constraining Silicate Weathering During the Middle Eocene Climatic Optimum (MECO) Using Radiolarian Ge/Si

by

Olivia R. Laub, Master of Science

Utah State University, 2023

Major Professor: Dr. Donald Penman
Department: Geosciences

Silicate weathering is one of Earth's most important processes and is in large part why our planet has remained hospitable for billions of years. To understand how silicate weathering regulates global temperatures, investigation into past periods of elevated temperatures is needed. One such period is the Middle Eocene Climatic Optimum (MECO) that occurred around 40 million years ago. During the MECO, silicate weathering seems to fail to control global temperatures, resulting in higher temperatures lasting for hundreds of thousands of years longer than comparable periods of warming. The MECO also deviates from other Paleogene warming events in its lack of a carbon isotope excursion, an indicator of a perturbation to the carbon cycle, and its prolonged decrease in carbonate preservation. The abnormal behavior of the carbon cycle during the MECO points to unusual behavior of the silicate weathering feedback during this event. I used the ratio of the elements germanium and silicon (Ge/Si) of siliceous microfossils to determine how silicate weathering changed across the MECO. When siliceous plankton build their tests, they incorporate ions from the surrounding seawater, thus recording the

relative concentrations of Ge and Si. Seawater Ge/Si is controlled by the mixing of continental inputs from silicate weathering, which have relatively low Ge/Si, and hydrothermal inputs, which have relatively high Ge/Si. On MECO-timescales, we can assume hydrothermal inputs remain constant, so a change in seawater Ge/Si would reflect a change in the weathering flux. If silicate weathering intensified during the MECO we would expect to see decreasing seawater Ge/Si values and the opposite if silicate weathering decreased. I found that Ge/Si values rose until the peak-MECO, implying that the weathering flux decreased. This result contradicts a predicted increase in silicate weathering in response to a warming climate. I suggest that instead, diminished silicate weathering acts as a driver of climate change for the MECO, explaining the differences between the MECO and other warming events. This study will increase our understanding of not only the Earth's response to a singular warming event, but also provide context for how the Earth is and will continue to respond to rising temperatures due to anthropogenic carbon emissions.

(70 pages)

PUBLIC ABSTRACT

Constraining Silicate Weathering During the Middle Eocene Climatic Optimum (MECO) Using Radiolarian Ge/Si

Olivia R. Laub

Silicate weathering has long been considered a fundamental component of the earth system and has been cited as one of, if not the primary stabilizing feedback for climate. However, recent work has shown that the role of silicate weathering in the climate system is more complicated and dynamic than previously assumed. In this study I examine the role of weathering in the enigmatic warming event, the Middle Eocene Climatic Optimum (MECO) that occurred approximately 40 Ma. This event works as a good case study as there are multiple features of the MECO that differentiate it from other warming events that occur around the same time. Using a relatively neglected proxy, the ratio of germanium to silicon (Ge/Si) of siliceous microfossils, I show that silicate weathering does not always correlate with temperature. I suggest that weathering may have instead been the driver of the observed warming during the MECO. This study will increase our understanding of not only the Earth's response to a singular warming event, but also provide context for how the Earth is and will continue to respond to rising temperatures due to current carbon emissions.

ACKNOWLEDGMENTS

First and foremost, I would like to thank my major advisor, Dr. Donald Penman, for his continued guidance and insight that has not only helped me in producing this thesis but also helped me grow as a researcher. I would also like to thank my committee members Dr. Carol Dehler and Dr. Tammy Rittenour for their feedback and suggestions for directions to take my research in.

I am also grateful to have had the opportunity to work alongside a fantastic lab group. I am indebted to Whitney Greaves and Dr. Audrey Warren for their help in picking countless radiolarians and troubleshooting the ICP-MS with me. I also need to thank Chels Howard and Samina Anee for being there to bounce ideas off of and as a constant source of support. I also want to thank Dr. Fen-Ann Shen for her help in operating the SEM at Utah State's Core Microscopy Lab. I will never tire of looking at the beautiful images of Radiolaria she helped me produce. Finally, I am eternally grateful to my friends, family, and my dog, Deccan, for being there for me throughout this process.

I am appreciative of IODP for providing the samples used in this study. Support for this research comes from Utah State University's Office of Research and Geoscience Department's Outstanding MSc Researcher Award and Summit Scholarship.

Olivia R. Laub

CONTENTS

LIST OF TABLES

Page

LIST OF FIGURES

INTRODUCTION

Recent human activities (from 1750 to 2019 CE) have released 700 ± 75 petagrams of carbon (PgC) into the atmosphere as carbon dioxide (CO_2), leading to approximately 1.0°C of global warming above pre-industrial levels via the greenhouse effect (Intergovernmental Panel on Climate Change [IPCC], 2018; IPCC, 2021). This warming is projected to increase to 1.5˚C between 2030 and 2052 if emissions continue at the current rate (IPCC, 2018). One way to understand the cascading impacts of this warming and to predict how the Earth's climate system will respond and recover is to study the paleoenvironmental sedimentary record of ancient warming events that featured similar climatic changes and Earth system feedbacks. One such event is known as the Middle Eocene Climate Optimum, or MECO, which occurred ~40 million years ago (Ma) (Figure 1; Bohaty and Zachos, 2003). This warming event is identified by a ~500 thousand year gradual decrease in benthic foraminiferal oxygen isotopic composition ($\delta^{18}O$), interrupting the long-term cooling trend that followed the Early Eocene Climatic Optimum (EECO, 52-50 Ma) (Zachos et al., 2001).

The Paleogene features multiple warming events, including the MECO as well as the Paleocene-Eocene Thermal Maximum (PETM, ~56 M). The PETM is one of the most pronounced and comprehensively studied warming events in the geologic record. First identified as an abnormally large foraminiferal carbon and oxygen excursion by Kennett and Stott (1991), the PETM is now recognized as a globally extensive event that affected both the marine and terrestrial realms (Figure 1; Koch et al., 1992) and is seen as the quintessential hyperthermal event. Hyperthermal refers to geologically brief (timescales of 10^3 to 10^5 yr) events that are characterized by rapid global warming and prominent

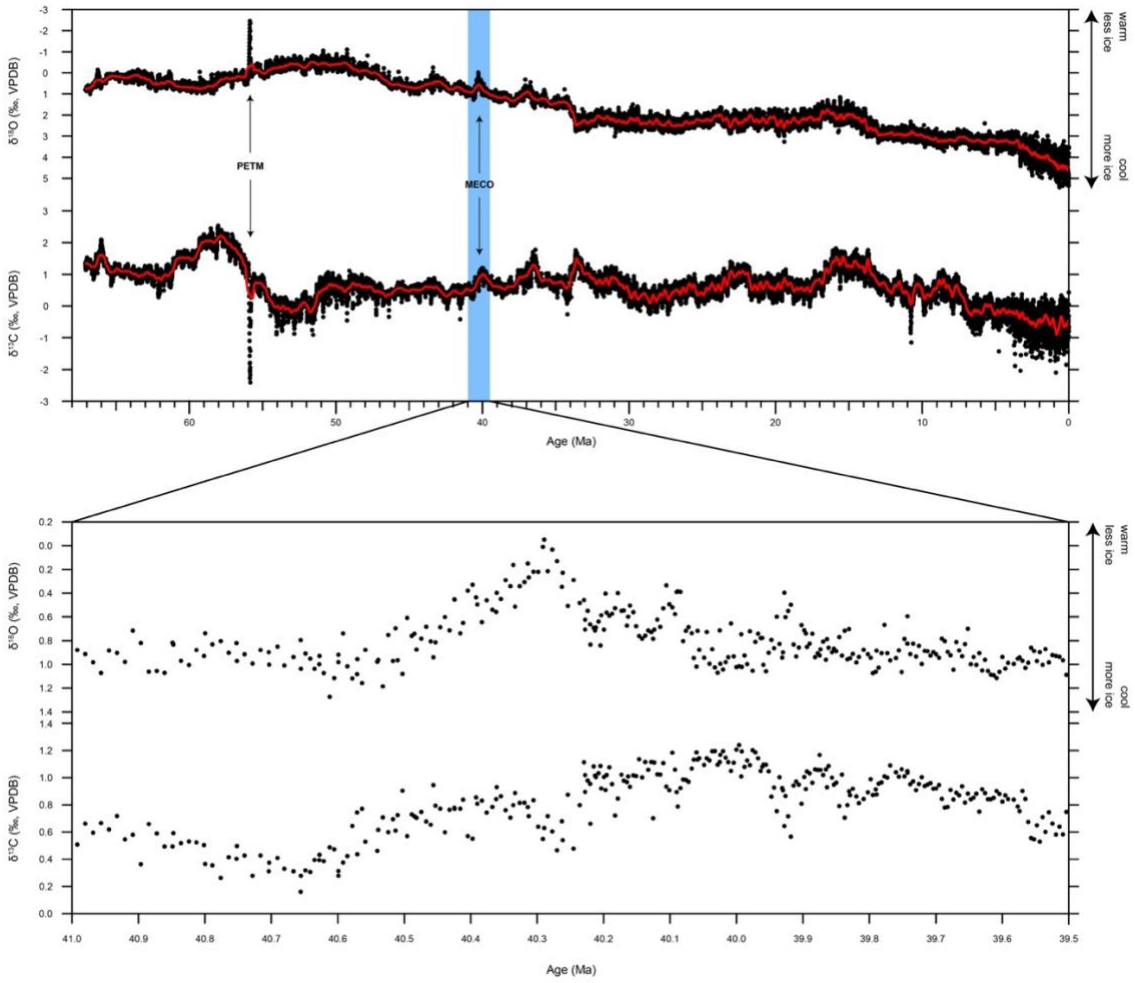

Figure 1. Benthic foraminiferal $\delta^{18}O$ and $\delta^{13}C$ across the Cenozoic and MECO. The uppermost plot shows $\delta^{18}O$ and $\delta^{13}C$ values from Westerhold et al. (2020), shown with black circles. A 100-point moving mean is shown with a red line. The PETM and MECO events are indicated by black arrows. The lower plot displays the $\delta^{18}O$ and $\delta^{13}C$ values in the blue shaded region of the upper plot.

negative stable carbon isotope ($\delta^{13}C$) excursions (CIE) that imply a large injection of depleted carbon into the ocean-atmosphere system (Dickens, 2009). During the PETM, global temperatures increased by several degrees (Kennett and Stott 1991; Zachos et al., 2001; Tripati and Elderfield, 2005; Zachos et al., 2006; Sluijs et al., 2011; Dunkley-Jones et al., 2013) and carbon isotope values dropped by 2-6‰ that likely required the release of thousands of gigatons of depleted carbon (Figure 1; McInerney and Wing, 2011). This resulted in a shift in ocean circulation (Nunes and Norris, 2006), ocean acidification (Penman et al., 2014; Babila et al., 2016; Babila et al., 2018), a shoaling of the carbonate compensation depth (CCD) (Zachos et al., 2005; Zeebe et al., 2009), modification of the hydrologic cycle (Tipple et al., 2011), and various impacts on both terrestrial and marine biota (e.g., Gingerich 1989; Koch et al., 1992; Thomas, 1998; Gingerich, 2001; Wing et al., 2005; Sluijs et al. 2007; Thomas, 2007).

While the MECO resembles the PETM and other Paleogene hyperthermals in some ways, it also bears stark differences that separates it from these other events. The first characteristic that sets the MECO apart from hyperthermals like the PETM is the duration of the event. One of the key features of hyperthermals is the rapid warming that marks the start of the event, such as the PETM where warming appears geologically instantaneous (likely within 10 kyr; e.g., Zachos et al., 2001; Kirtland Turner et al., 2017). The MECO, in comparison, features gradual warming over ~500 kyr followed by a rapid (~50 kyr) cooling and a return to pre-event temperatures over the subsequent ~200 kyr (Figure 2; Bohaty and Zachos, 2003; Bohaty et al., 2009). Another distinguishing feature of the MECO is its lack of CIE. The PETM has a CIE that mirrors its oxygen isotope excursion in timing and in magnitude (Figure 2). In contrast, $\delta^{13}C$

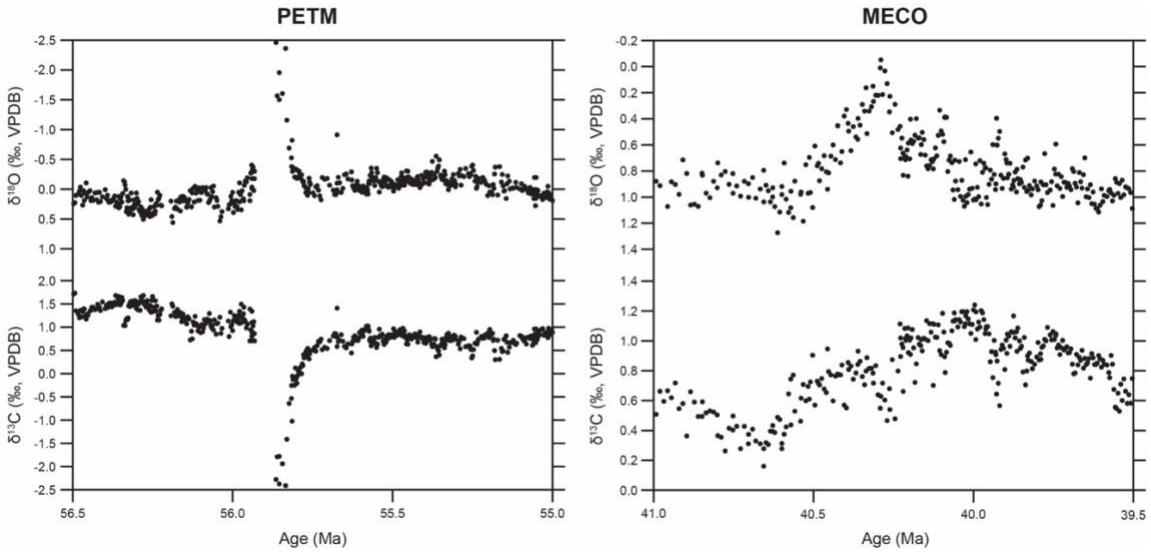

Figure 2. Comparison of PETM and MECO benthic foraminiferal $\delta^{18}O$ and $\delta^{13}C$ values. Isotopic values shown with black circles from Westerhold et al. (2020). Both plots cover 1.5 million years but possess different y-scales to account for the different isotopic shifts. The PETM has an abrupt $\delta^{18}O$ excursion and a corresponding $\delta^{13}C$ excursion while the MECO experiences a more gradual decrease in $\delta^{18}O$ values and does not have an associated drop in $\delta^{13}C$ values.

values during the MECO remain relatively stable or even elevated until peak warming, at which a brief negative CIE of ~0.5 ‰ occurs in some, but not all, records (Figure 2; Bohaty and Zachos, 2003; Bohaty et al., 2009). The final major distinction of the MECO is the prolonged decrease in the preservation of deep-sea carbonates across the event. Lowered deep-sea sedimentary carbonate content is observed in both the PETM and the MECO, but the duration and response differ between the events (Bohaty and Zachos, 2003; Zachos et al., 2005; Bohaty et al., 2009; Penman et al., 2014; Babila et al., 2016; Penman et al., 2016; Babila et al., 2018). For the PETM, this decrease is attributed to ocean acidification from elevated CO_2 concentrations associated with the initial carbon released during the CIE that reduced seawater carbonate saturation and led to a shoaling of the lysocline and CCD (Zachos et al., 2005; Pagani et al., 2006; Gibbs et al., 2010; Penman et al., 2014; Penman et al., 2016). Immediately following the PETM CIE body, though, there is an observed "carbonate overshoot" during which a period of carbonate oversaturation led to an over-deepening of the CCD and increased carbonate burial (Kelly et al., 2005; Kelly et al., 2012; Penman et al., 2016). The MECO also experiences decreased carbonate burial, but unlike the PETM, this shoaling of the CCD persists for several hundred thousand years (Bohaty and Zachos, 2003; Bohaty et al., 2009; Sluijs et al., 2013) and following the MECO there is no evidence of an overshoot (Bohaty et al., 2009; Sluijs et al., 2013).

Previous authors (e.g., van der Ploeg et al., 2018) have proposed a weaker silicate weathering feedback as a potential reason for the differences between the MECO and hyperthermal events like the PETM. The silicate weathering feedback has long been considered the principal stabilizer for long-term climate (Garrels et al., 1976; Walker et

al., 1981). During periods of elevated temperature and atmospheric CO_2 concentrations, the chemical weathering of continental silicate rocks is thought to accelerate, consuming CO_2 as part of the weathering process. The dissolved weathering products are transported to the oceans where they are precipitated as marine carbonates and silica. These products also act as an alkalinity supply, reducing seawater acidification from elevated CO_2 concentrations. A generalized chemical reaction for the weathering of the mineral wollastonite (1) can be used to illustrate silicate weathering:

$$CaSiO_3 + 2CO_2 + H_2O \rightarrow Ca^{2+} + 2HCO_3^- + SiO_2 \quad (1)$$

The weathering products are then transported to the oceans where they will precipitate as new carbonate minerals (2) and eventually be buried:

$$Ca^{2+} + 2HCO_3^- \rightarrow CaCO_3 + CO_2 + H_2O \quad (2)$$

This process in sum (3) leads to the overall consumption of atmospheric CO_2 and, due to the greenhouse effect, lowers global temperatures:

$$CaSiO_3 + CO_2 \rightarrow CaCO_3 + SiO_2 \quad (3)$$

In contrast, during cooler periods silicate weathering reduces, leading to a buildup of atmospheric CO_2 and increasing temperature. In addition to moderating atmospheric CO_2 levels and Earth's climate on longer timescales, this feedback has been proposed as the primary mechanism for climatic recovery following transient climatic and carbon cycle perturbations like the PETM and other hyperthermals (e.g., Dickens et al., 1997; Zachos et al., 2005; Kelly et al., 2005; Panchuk et al., 2008; Zeebe et al., 2009; Penman, 2016; Penman et al., 2016).

Based on current understanding of carbon cycle dynamics from past events like the PETM, on timescales of the MECO (~500 kyr) the silicate weathering feedback

should have prevented the three main irregularities of the MECO from occurring. If silicate weathering operated as expected, the feedback should have prevented the observed prolonged period of warming during the MECO by drawing down atmospheric CO_2. Typically, the large injection of carbon into the ocean-atmosphere system at the start of a hyperthermal event would overwhelm the system, resulting in an observed CIE and widespread carbonate dissolution in the marine sediment record until silicate weathering could re-engage to drawn down atmospheric CO_2 and act as an alkalinity supply to the oceans. Instead, during the MECO no CIE, and thus no initial injection of carbon, is observed and pH levels continue to decrease through the peak-MECO (Henehan et al., 2020). This contradiction between proxy evidence and model expectations has earned the event the nickname the 'middle Eocene carbon cycle conundrum' (Slujis et al., 2013). To resolve this discordance, an investigation into the behavior of silicate weathering across the MECO is necessary.

A previously published osmium isotope ($^{187}Os/^{188}Os$) record shows reduced $^{187}Os/^{188}Os$ during the MECO that was interpreted to reflect a diminished weathering response (van der Ploeg et al., 2018). $^{187}Os/^{188}Os$ can be used as a paleoweathering proxy because the ratio recorded in marine sediments reflects seawater $^{187}Os/^{188}Os$ that is controlled by the relative contributions of the main weathering fluxes to the ocean (Percival et al., 2016). The residence time of Os in seawater is 10 to 50 thousand years, meaning it is long enough to be well mixed throughout the oceans while also being short enough to record geologically abrupt changes such as the MECO (Peucker-Ehrenbrink and Ravizza, 2000). ^{187}Os is a radiogenic isotope produced from the decay of the radioactive isotope of rhenium (^{187}Re; Percival et al., 2016). Due to the differences in the

compatibilities of Os and Re in silicate melts, primitive lithospheric mantle is more enriched in Os/Re than continental crust (Percival et al., 2016). Thus, once a melt solidifies, the relatively higher quantities of radioactive Re in continental rocks will decay to ^{187}Os, making the source more radiogenic in comparison to sources that reflect primitive lithospheric mantle Os/Re ratios, such as hydrothermal activity at mid-ocean ridges, highly fresh mantle-derived basalts, and extraterrestrial sources (Peucker-Ehrenbrink and Ravizza, 2000). This suggests that a sediment with a lower $^{187}Os/^{188}Os$ ratio, such as those from the MECO, reflects a relatively lower supply from continental sources due to decreased weathering rates (Cohen et al., 1999). While there is also a possibility that one of the other potential influences on $^{187}Os/^{188}Os$, namely a rise in hydrothermal activity or an increase in the weathering of mantle-derived rocks (e.g., Lu et al., 2017), could be controlling the observed trends, the potential for counterintuitively diminished weathering during the MECO necessitates further investigation.

The germanium to silicon ratios (Ge/Si) of siliceous microfossils has the potential to reconstruct changes in continental weathering during the MECO. Due to having similar chemical properties, such as similar ionic radii, covalent Ge–O and Si–O bond lengths, and the outer electronic structures, Ge substitutes for Si at a ratio of ~1 Ge atom per 1,000,000 Si atoms in virtually all Si-bearing phases (Froelich et al., 1992). Despite following similar biogeochemical cycles, the differences in behavior of the two elements allows the elemental ratio to be used as a geochemical tracer, much like a pseudo-isotope of Si (e.g., Shemesh et al., 1989). Seawater Ge/Si is controlled by the collective input and removal fluxes of Ge and Si to the oceans (Figure 3). Inputs of Ge and Si can be simplified to continental and hydrothermal fluids (Figure 4a; Froelich and Andreae, 1981;

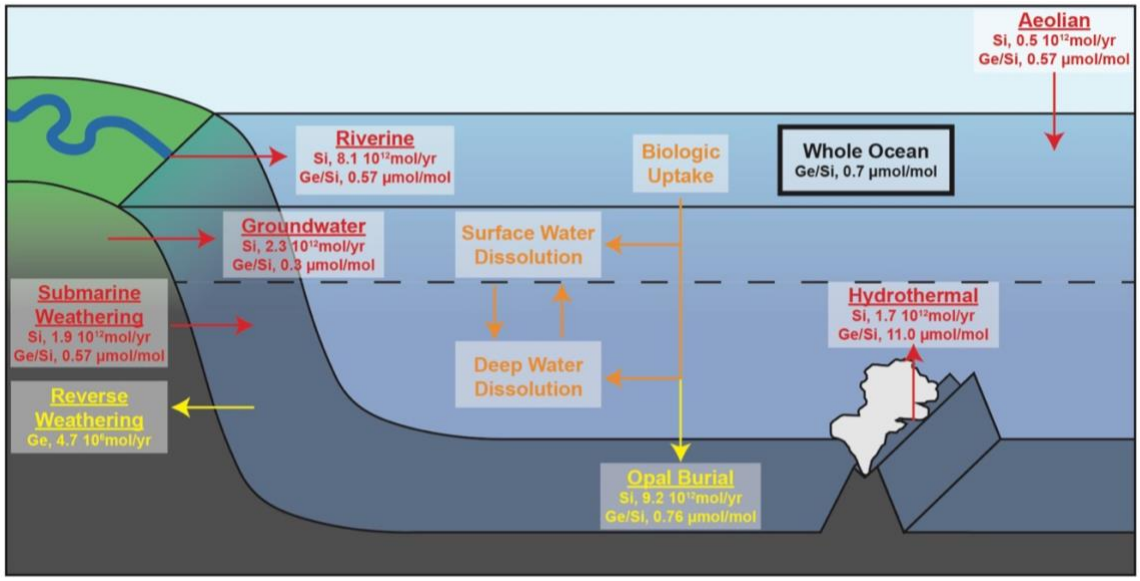

Figure 3. Schematic of Ge and Si fluxes to, from, and within the oceans. The ocean is separated into surface (upper ~100 m) and deep reservoirs. Red text and arrows denote the major fluxes of Ge and Si to seawater, orange text and arrows show internal ocean processes, and yellow text and arrows show the major fluxes of Ge and Si from the seawater into marine sediments. Each flux has an associated Si flux in Tmol/yr and Ge/Si value (from which the Ge flux is calculated). The exception is the reverse weathering flux where Ge is preferentially sequestered, so only a Ge flux is noted. Flux and Ge/Si values are from Froelich et al. (1992), Mortlock et al. (1993), Hammond et al. (2004), Sutton et al. (2010), Tréguer and De La Rocha (2013), and Tréguer et al. (2021).

Froelich et al., 1985; Mortlock et al., 1993; Baronas et al., 2016; Tréguer et al., 2021). The average Ge/Si of silicate rocks narrowly varies between 1.5 and 3 μmol/mol (Rouxel et al., 2006), reflecting the only minor fractionation that occurs between Ge and Si during fractional crystallization (De Argollo and Schilling, 1978; Rouxel et al., 2006). During the weathering process, secondary minerals preferentially sequester Ge (Kurtz et al., 2002), leading to the Ge/Si of continental fluids ranging from 0.3 to 1.2 μmol/mol with an average of ~0.6 μmol/mol (Figure 4a; Froelich et al., 1985; Mortlock and Froelich 1987; Froelich et al., 1992). In contrast, the Ge/Si of hydrothermal fluids ranges between 8 and 14 μmol/mol (Figure 4a; Mortlock et al., 1993; Elderfield and Schultz, 1996). This large disparity in Ge/Si values is due to mineral-fluid interactions and Ge not being sequestered in the high-temperature secondary alteration minerals that form within the hydrothermal vent plumbing, leaving the resulting solution highly enriched in Ge (Mortlock and Froelich, 1986; Mortlock et al., 1993). The mixing of these two main input fluxes results in a modern seawater Ge/Si value of ~0.7 μmol/mol (Froelich and Andreae, 1981).

Measurements of Ge/Si throughout the ocean are nearly constant with no evidence for any vertical or horizontal variation, implying that Si and Ge are highly mixed in seawater (Froelich and Andreae, 1981). Therefore, siliceous organisms such as diatoms, radiolarians, and sponge spicules that build their tests using ions from the surrounding seawater can be used as recorders of whole-ocean Ge/Si. Laboratory culture experiments have shown there is minimal discrimination against Ge during Si uptake from the surrounding water in diatoms (Azam, 1974; Froelich et al., 1992; Bareille et al., 1998; Ellwood and Maher, 2003; Sutton et al., 2010). This result is consistent with

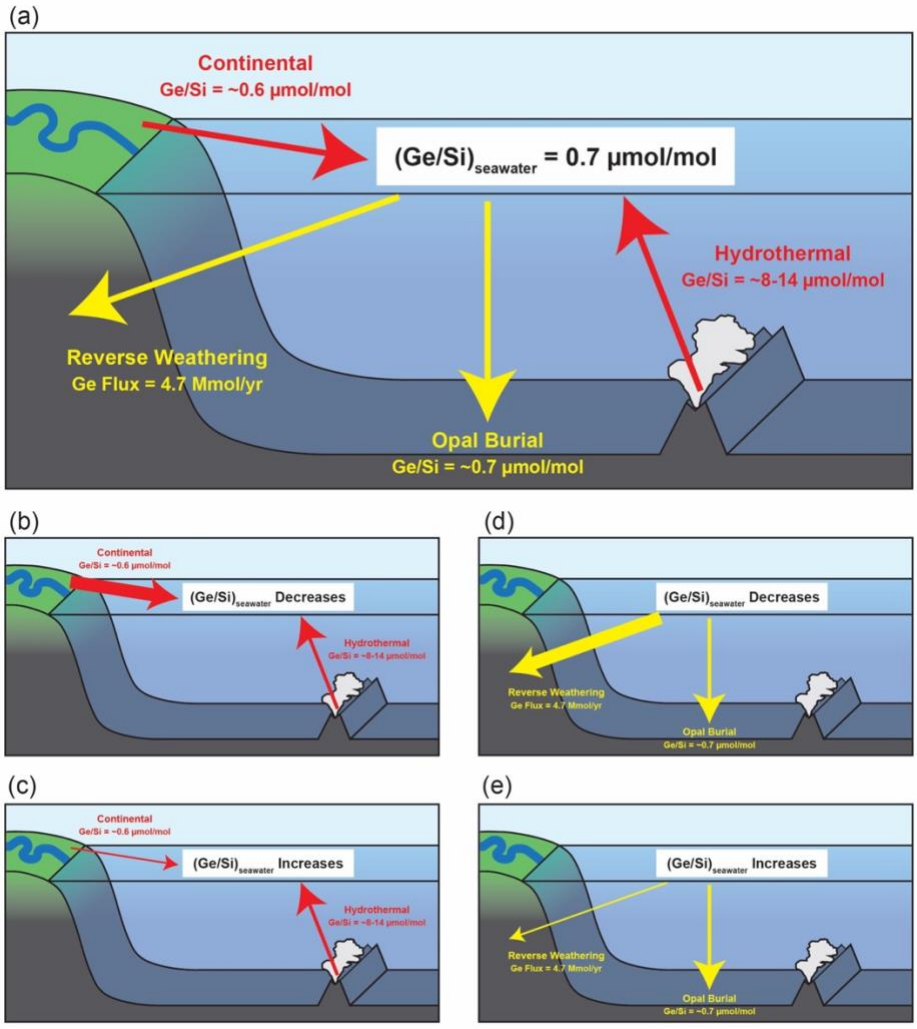

Figure 4. Schematic of changes to seawater Ge/Si following changes in the simplified fluxes to and from the ocean. (a) The simplified input fluxes, continental (average Ge/Si = ~0.6 µmol/mol) and hydrothermal fluids (Ge/Si = ~8-14 µmol/mol), and sinks, opal burial (Ge/Si = ~0.7 µmol/mol) and reverse weathering (Ge flux = 4.7 Mmol/yr) that result in the modern seawater Ge/Si value of 0.7 µmol/mol. (b – c) Schematic of input-controlled Ge/Si hypothesis where the relative strength of the continental and hydrothermal fluxes primarily controls the Ge/Si of seawater. (b) An increase in the continental flux would result in lower seawater Ge/Si values, due to the relatively lower values from the continents, while (c) a decrease in the continental flux would result in higher seawater Ge/Si. (d – e) Schematic of input-controlled Ge/Si hypothesis where the seawater Ge/Si is controlled by the relative strength of opal burial and reverse weathering. (d) This hypothesis postulates that an increase in reverse weathering, which preferentially sequesters Ge, would lead to a decrease in seawater Ge/Si while (e) a relative decrease would increase seawater Ge/Si. Flux values are from Froelich et al. (1992), Mortlock et al. (1993), Hammond et al. (2004), and Sutton et al. (2010).

diatoms collected from marine sediment core tops that record the Ge/Si of modern seawater (Shemesh et al., 1989). Radiolarians and sponge spicules have shown some evidence of a constant, subtle fractionation against Ge but remain useful recorders of trends in past biogeochemical cycling (Shemesh et al., 1989; Froelich et al., 1992; Ellwood et al., 2006; Baronas et al., 2016).

Siliceous microfossils collected from marine sediment cores can therefore be used to construct a record of past fluctuations in whole-ocean Ge/Si (e.g., Shemesh et al., 1989; Bareille et al., 1998; Lin and Chen, 2002). There are two main hypotheses used to interpret Ge/Si records. The first assumes that the dominant control on seawater Ge/Si is the relative strengths of the main input fluxes: continental sources and hydrothermal fluids (e.g., Froelich and Andreae, 1981; Shemesh et al., 1989; Froelich et al., 1992; Elderfield and Schultz, 1996). On timescales of the MECO, we can assume hydrothermal inputs remain constant, suggesting that a change in seawater Ge/Si reflects a change in the continental flux, and thus silicate weathering (Froelich and Andreae, 1981; Shemesh et al., 1989; Froelich et al., 1992; Elderfield and Schultz, 1996). As continental sources have low Ge/Si, if the delivery of dissolved silica from the continents were to increase relative to a previous state, we would expect seawater Ge/Si to decrease (Figure 4b). Conversely, reduced continental inputs from diminished silicate weathering would result in increased seawater Ge/Si (Figure 4c). As the residence time of Si and Ge are both approximately 8,000 years, we would expect to see a noticeable shift in whole ocean values across the MECO if the relative strengths of the input sources changed.

A second hypothesis suggests that a main control on seawater Ge/Si is the strength of the elemental sinks, rather than the inputs. The primary sinks for Ge and Si

are biogenic opal burial and the sequestration of primarily Ge in authigenic clay minerals at the sediment-water interface, particularly in marginal environments (Hammond et al., 2000; King et al., 2000; McManus et al., 2003; Hammond et al., 2004). The original assumption was that biogenic opal burial was the principal sink for both Ge and Si, but a discrepancy in balancing the global marine Ge budget seemingly requires a greater removal flux than what is observed in opal burial alone (Mortlock et al., 1993; Elderfield and Schultz, 1996; Hammond et al., 2000; King et al., 2000; McManus et al., 2003). Investigation into this "missing" Ge sink led to the discovery of Ge removal in the porewaters of reducing sediments on continental margins and in suboxic basins (Hammond et al., 2000; King et al., 2000; McManus et al., 2003; Baronas et al., 2016; Baronas, 2017). Low Ge/Si of porewaters in those specific environments suggests that dissolution of siliceous material at the sediment-water interface drives the precipitation of some heretofore unidentified authigenic mineral(s) which preferentially sequesters Ge, lowering porewater (and subsequently seawater) Ge/Si (Murnane et al., 1989; Hammond et al., 2000; King et al., 2000; McManus et al., 2003; Hammond et al., 2004). This alternative hypothesis reasons that during warmer climates a greater proportion of siliceous tests will dissolve before reaching the seafloor where Ge is removed, thus increasing seawater Ge/Si (Figure 4d), while cooler global temperatures lead to decreasing Ge/Si (Figure 4e; Hammond et al., 2004). Overall, this hypothesis argues that changes in recorded opal Ge/Si is controlled by temperature as well as varying input fluxes of silicate weathering and hydrothermal input.

This second hypothesis introduced new complexities of the Ge/Si system that resulted in the lack of attention given to the proxy in the past few decades. Froelich and

Andreae (1981) first suggested that Ge/Si could be used as a proxy for weathering processes. The following two decades saw the proxy applied mainly to glacial-interglacial cycles (e.g., Mortlock and Froelich, 1987; Shemesh et al., 1989; Froelich et al., 1992; Bareille et al., 1998). After Hammond et al. (2000) and subsequent studies (e.g., King et al., 2000; McManus et al., 2003; Hammond et al., 2004) identified the potential secondary control on seawater Ge/Si, the proxy became less widely applied. Recently, however, the proxy has matured, prompting renewed interest in applying Ge/Si to more time periods and investigating the biogeochemical cycle of Ge and Si closer (e.g., Opfergelt et al., 2010; Qi et al., 2019; Li, 2019; Wang et al., 2022). The purpose of this study is to both explore the application of Ge/Si to deep time records and to investigate what the proxy can tell us about silicate weathering across the enigmatic MECO event.

METHODS

The MECO at Site U1511

Siliceous microfossils were isolated from sediment cores collected from the Tasman Abyssal Plain at Site U1511 during IODP Expedition 371 (Figure 5). Site U1511 consists of three lithologic units spanning approximately 560 m of Pleistocene to Paleocene clay and diatomite. Unit II comprises a Middle Eocene diatomite with varying amounts of other biosilica and clay. A well-resolved magnetostratigraphic age model for this Unit (Dallanave and Chang, 2020) identifies MECO-aged sediment within Core U1511B-16R. Sections 16R-4 and 16R-5 (corresponding to approximately 266.5 to 264.2 meters below seafloor, mbsf) contain the base of magnetochron C18n, the

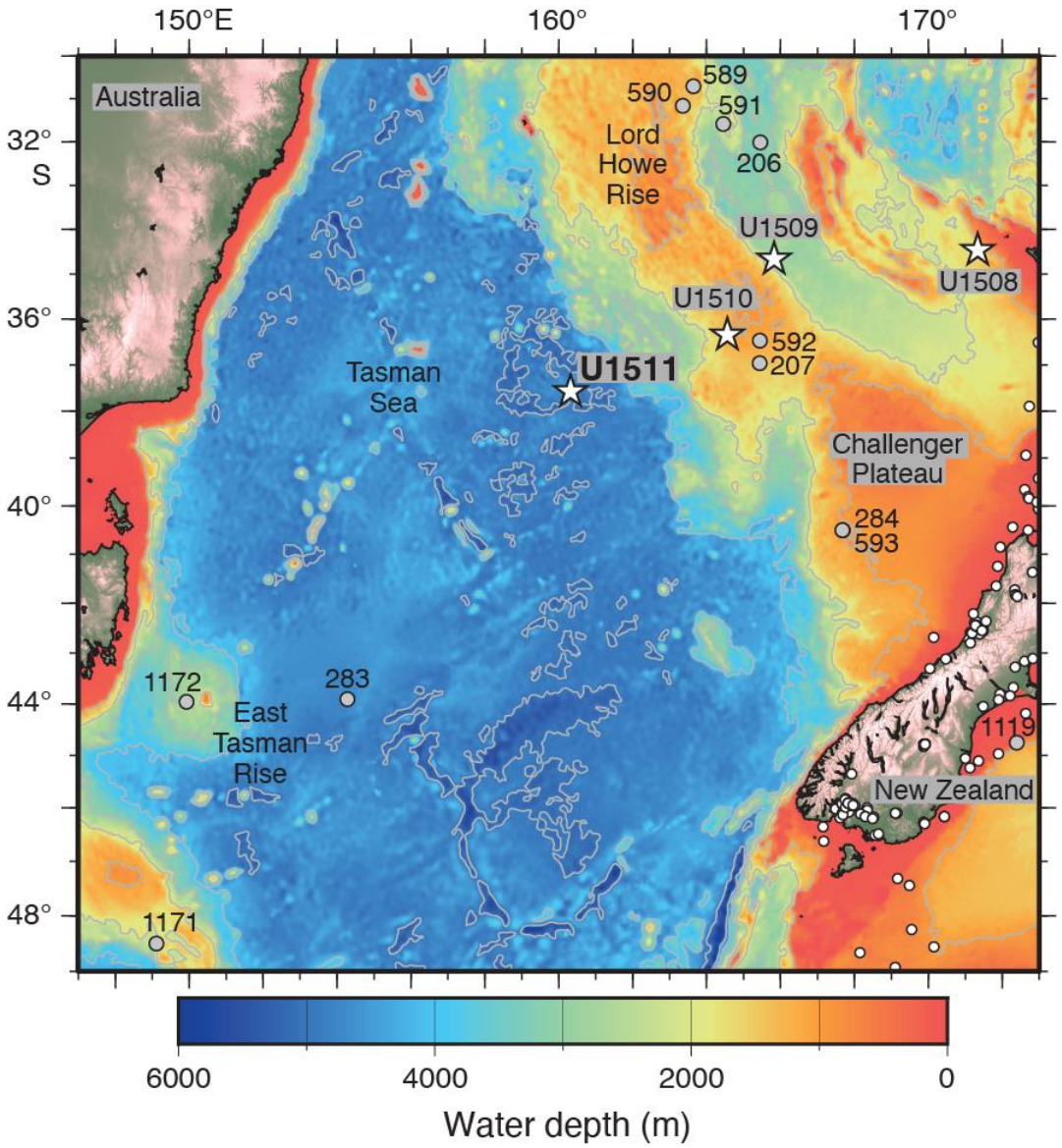

Figure 5. Map showing bathymetry of the Tasman Sea Abyssal Plain and major regional boreholes. IODP Site U1511 is bolded and starred. Other IODP Expedition 371 borehole sites are also starred while the white dots denote petroleum borehole sites and gray dots show Deep Sea Drilling Project (DSDP) and Ocean Drilling Program (ODP) sites. Figure from Sutherland et al. (2019).

magnetostratigraphic marker of the MECO (Dallanave and Chang, 2020). In addition to magnetostratigraphy, core-scanning X-ray fluorescence data show elevated aluminum, iron, and manganese concentrations between 266.57–264.85 mbsf that have been interpreted as related to changing abyssal circulation and acidification during the MECO (Cornaggia et al., 2020).

When investigating trends at solely IODP Site U1511, we assigned magnetostratigraphic chron-depth points identified by Dallanave and Chang (2020) to the most recent astrochronologically-calibrated magnetostratigraphic reversal ages from Westerhold et al. (2020). However, in order to compare our record to published benthic foraminifera $\delta^{18}O$ records on a common timescale, a separate age model for Site U1511 based on the magnetostratigraphic tie points developed by Bohaty et al. (2009) was used.

Specimen Isolation

To disaggregate raw samples, a solution of 200 ml of deionized water with 0.5% sodium hexaphosphate, a clay dispersant, was added to oven-dried diatomite samples in 500 mL bottles before being transferred to an orbital shaker table set to 180 rpm. All samples were initially weighed before the disaggregating solution was added. The solution was gently agitated until no large aggregates of solid material could be observed. Siliceous material was then physically separated from the clay by wet sieving at 125, 63, 38, 25, and 10 μm.

Two orders of Radiolaria, *Spumellaria* and *Nassellaria*, were targeted from the >125 μm size fraction (Figure 6). All spumellarian individuals are from the family *Actinommidae* while all nassellarian individuals were from the family *Theoperidae* (for

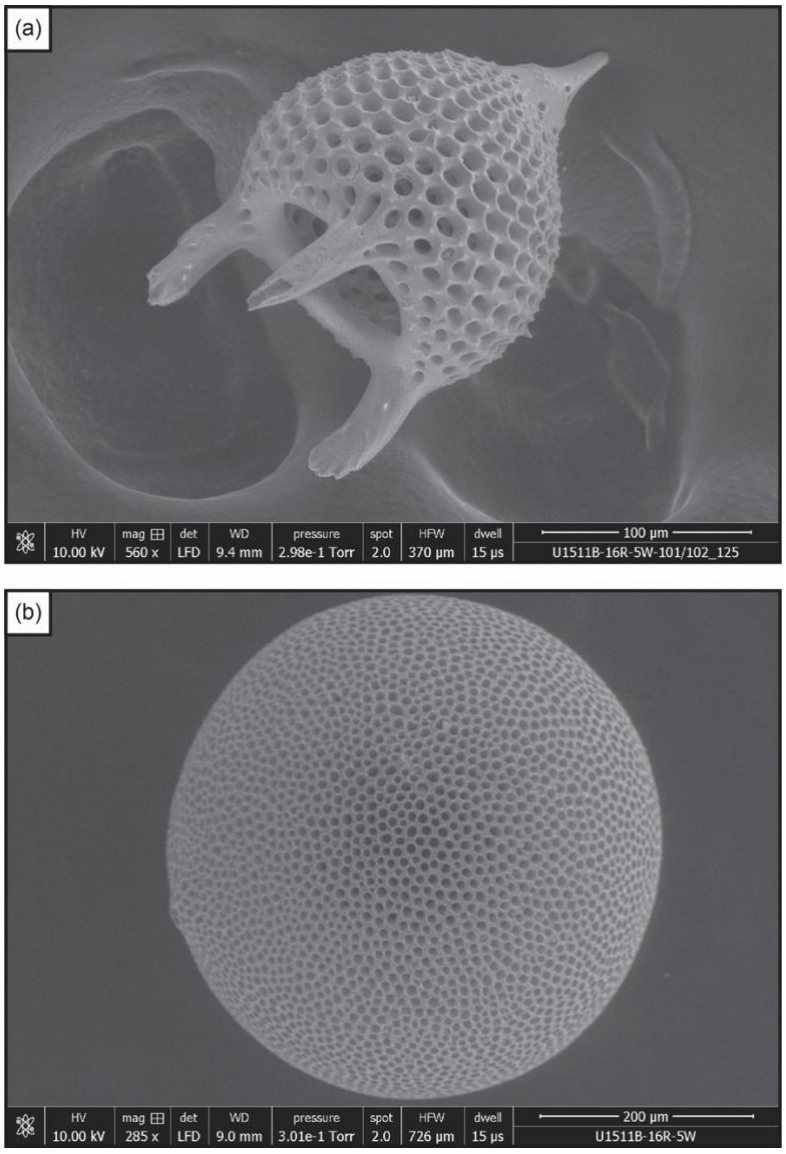

Figure 6. SEM images of targeted radiolarian morphologies. (a) A nassellarian morphospecies in the family *Theoperidae*. (b) A spumellarian morphospecies in the family *Actinommidae*.

morphotypes targeted see Figure 6). All radiolarian species are planktonic but have a depth range from surface to almost a kilometer (Lazarus et al., 2020). The specific depth range of targeted specimen is unknown.

Individual specimens were chosen under a stereoscope according to morphology and by prioritizing clear over recrystallized specimen. Approximately 200 μg of SiO_2 (40-100 individuals) was isolated from a total of 58 sediment samples that span the MECO (Cores 16 and 17; 261.025 to 278.025 mbsf) at 10 – 25 cm resolution.

Sample Cleaning

Following physical separation, the samples underwent chemical cleaning to remove clay contamination identified during scanning electron microscope (SEM) imaging and energy dispersive spectroscopy (EDS) analyses. A trial run on the inductively coupled plasma mass spectrometer (ICP-MS) revealed that uncleaned samples had a larger scatter and consistently higher Ge/Si values (Figure 7). This is likely due to the higher retention of Ge in clay contaminants. To remove potential contamination, cleaning methods were developed based on a procedure designed for cleaning foraminifera (Barker et al., 2003). The foraminiferal procedure includes (1) repeated sonicating and rinsing in methanol and Milli-Q water to remove clays and fine particulate matter, (2) a reductive step using a hydrazine solution to remove metal-oxide coatings, and (3) an oxidative step with buffered hydrogen peroxide (H_2O_2) to remove any organic material. EDS analysis was performed on radiolarian samples that had underwent an individual cleaning step, the full procedure, or no cleaning to determine which resulted in the removal of Ge-rich surficial clay contamination (Figure 8). Clay

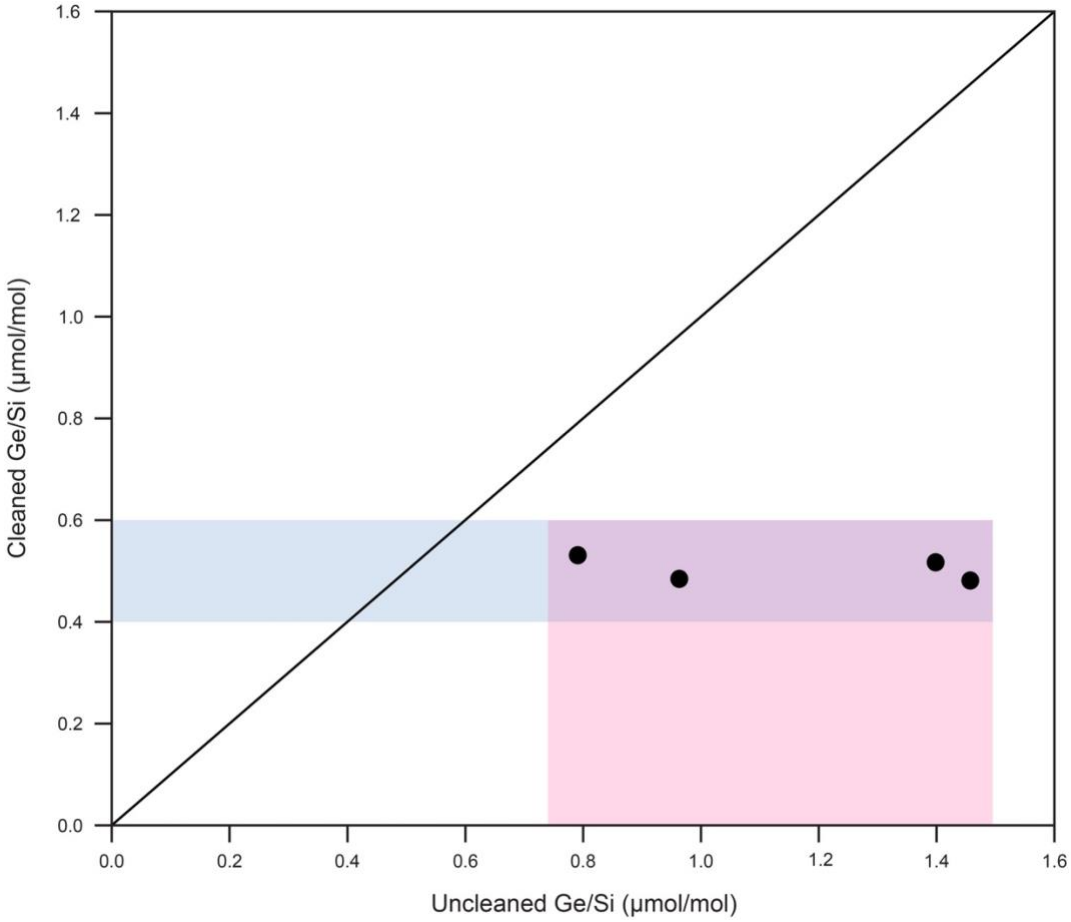

Figure 7. Comparison of resulting Ge/Si values from samples that underwent the full foraminiferal cleaning procedure and those that did not. The cleaning procedure included a sonication and methanol rinsing step to remove clays and fine particulate matter, a reductive step that used hydrazine solution to remove metal-oxide coatings, and an oxidative step with buffered hydrogen peroxide that removed organic material. The cleaned sample Ge/Si values had a much narrower range (blue shaded region) than the uncleaned samples (pink shaded region) that more closely resembled the modern and Pleistocene radiolarian Ge/Si range of 0.25 to 0.46 µmol/mol (Shemesh et al., 1988; Shemesh et al., 1989). Uncleaned samples also consistently returned higher Ge/Si values, indicating the presence of Ge-rich clay contaminants.

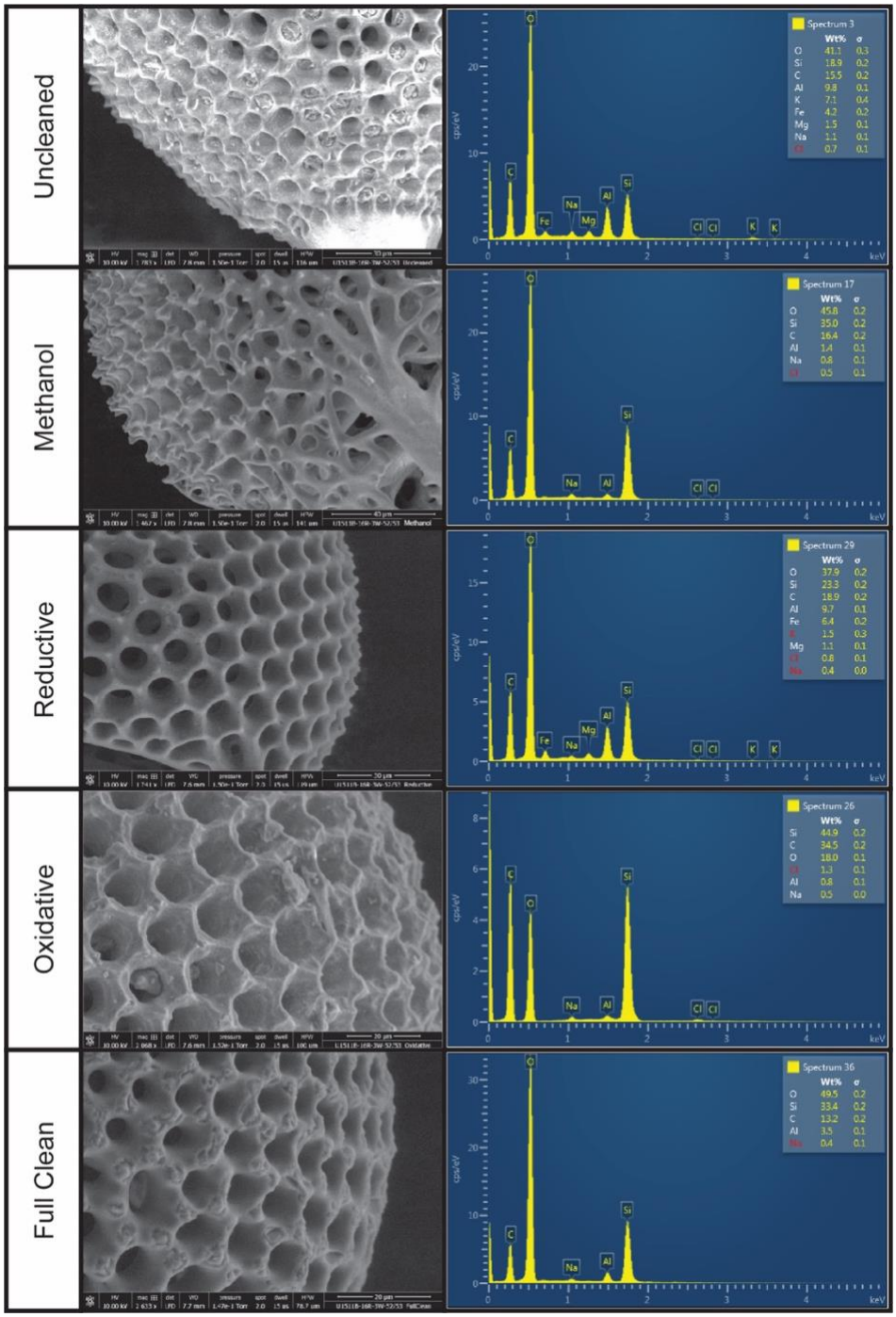

Figure 8. SEM and EDS analysis of specimen that were either uncleaned, solely sonicated and methanol-rinsed, solely underwent the reductive step, solely underwent the oxidative step, or underwent the entire cleaning procedure. EDS detection was used to investigate the specimen with the lowest weight percentage (Wt%) of aluminum (Al). Al Wt% was used as an indicator of clays. The abundances in the figure show the worst case scenarios for each specimen analyzed. SEM analysis revealed surficial pitting in the reductive and oxidative steps. Therefore, to prevent the loss of siliceous material while also removing the majority of clay contaminants, the cleaning procedure was reduced to a series of MQ water and methanol rinses interspersed with 30 seconds of sonication.

contamination was identified by aluminum (Al) weight percentage in EDS analysis. Each group also underwent SEM imaging that revealed surficial pitting of test surfaces following both the reductive and oxidative step (Figure 8). To prevent the loss of siliceous material for analysis, the cleaning procedure was reduced to a series of Milli-Q water and methanol rinses interspersed with 30 seconds of sonication. EDS analysis confirmed that the methanol rinsing step was sufficient to remove the majority of clay contaminants.

Ge/Si Analysis

Samples were then dissolved in 100 µL of 5 M sodium hydroxide (NaOH, Sigma-Aldrich "semiconductor grade") at 70˚C for at least 48 hours. After no undissolved solid could be visually detected, the samples were neutralized and acidified to 0.5 M HNO_3 by adding 122 µL of 5 M HNO_3 and further diluted by adding 1028 µL of 0.5 M HNO_3. The solution was then transferred by micropipette to labeled, acid-cleaned 2 mL screw-top Cryovials, leaving behind the last 50 µL to avoid any undissolved solid material. Samples were then run on an Agilent 8900 triple-quadrupole inductively-coupled plasma mass spectrometer (QQQ-ICP-MS) to measure Ge and Si counts, as well as a suite of other elements (Li, B, Al, S, Ti, Mn, and Zn). Ge and Si were both measured in several different gas modes (with no gas, He, or O_2 added to the collision/reaction cell separating the two quadrupole mass filters). Samples were run alongside gravimetrically-prepared calibration standards spanning a range of known Ge/Si ratios, which were used to convert measured Ge and Si signals to calibrated Ge/Si values. A separate Ge/Si standard was used as a consistency standard (treated as an unknown) to monitor accuracy and long-

term precision. Ge/Si values for the consistency standard measured in O_2 mode usually produced the greatest precision, within 4-6% (1 standard deviation) across all analytical runs. However, using several combinations of Ge and Si gas modes resulted in comparable precision and accuracy. Approximately 28.4% of samples were run in duplicate (across multiple analytical runs) to evaluate consistency and to double-check apparent outliers. Following assessment, outlier values (7 out of the total of 154 Ge/Si analyses, all with anomalously high Ge/Si potentially indicating clay contamination) were removed and remaining sample duplicates were averaged (Table A1).

Box Model for Ge and Si

I designed a two-box model of the marine silicon and germanium cycle, closely resembling those developed by De La Rocha and Bickle (2005) and Fontorbe et al. (2020), using the program MATLAB to track Ge and Si fluxes to and from the ocean (Figure 9). This model simulates the steady-state inputs for both elements and various scenarios of perturbation and recovery (Table 1; Tréguer et al., 1995; Hammond et al., 2004; Tréguer and De La Rocha, 2013). The two boxes in the model represent the surface (upper 100 m) and deep ocean. Ge and Si are added to the surface ocean via riverine input (continental silicate weathering), removed via reverse weathering and biologic uptake, and released back to the water due to dissolution of opal material. In the deep ocean the main input flux is hydrothermal fluids, while Ge and Si are delivered from the surface water as opal rain and either added to the deep-sea reservoir via dissolution or removed from the model during burial. Additionally, Ge and Si are schematically exchanged between the surface and deep oceans due to upwelling and downwelling based

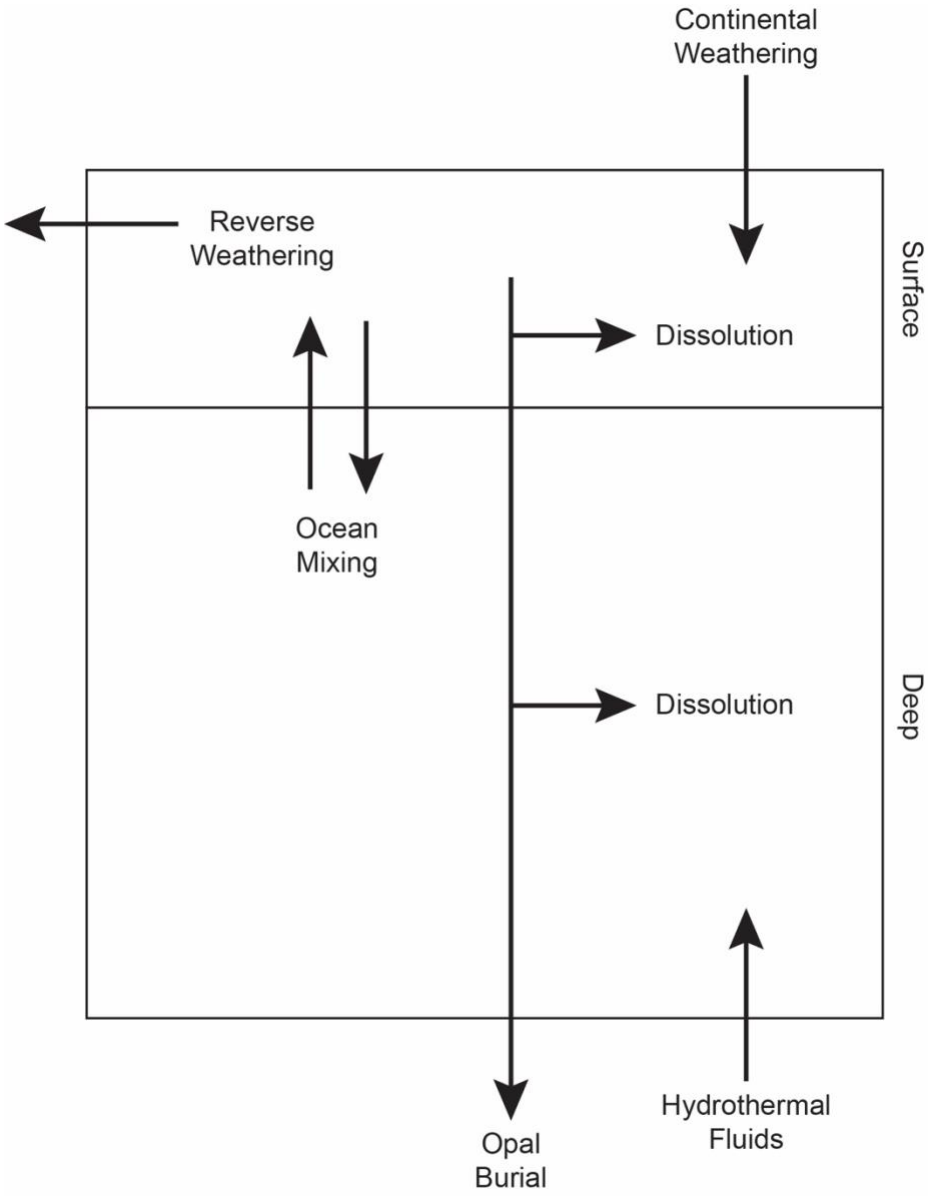

Figure 9. Schematic of two-box model used to simulate the response of ocean Ge/Si ratios to variations in input and output flux strengths. Figure modified from Fontorbe et al. (2020).

Table 1. Budgets of Si and Ge fluxes with associated Ge/Si values used in the geochemical box model.

	Si (Tmol/yr)	**Ge/Si (µmol/mol)**	**Ge (Mmol/yr)**
Inputs			
Continental	6.50[a]	0.50[b]	3.25[d]
Hydrothermal	0.60[c]	11.00[b]	6.60[d]
Sinks			
Biogenic Opal	7.10[e]	0.73[f]	5.15[g]
Reverse Weathering	--	--	4.70[b]

[a] Tréguer et al. (1995)
[b] Hammond et al. (2004)
[c] Tréguer and De La Rocha (2013)
[d] (Si flux)*(measured Ge/Si)
[e] Calculated to balance inputs
[f] Emerges from model
[g] (Si biogenic opal burial flux)*(seawater Ge/Si)

on a fixed oceanic mixing rate (De La Rocha and Bickle, 2005).

RESULTS

Ge/Si ratios measured on our Middle Eocene radiolarians range from 0.25 to 0.55 μmol/mol (Figure 10), very similar to the range measured in previous studies on modern and Pleistocene radiolarians of 0.25 to 0.46 μmol/mol (Shemesh et al., 1988; Shemesh et al., 1989). Across the MECO, the Ge/Si records of the two orders, *Spumellaria* and *Nassellaria*, exhibit similar Ge/Si trends with depth but spumellarian samples consistently have Ge/Si values 30% higher than nassellarian samples from the same depth (Figure 10). Across the MECO, spumellarian Ge/Si values range from 0.34 to 0.58 μmol/mol while nassellarian Ge/Si values range from 0.25 to 0.47 μmol/mol (Figure 10). At present, the cause of the Ge/Si offset between the two orders is unexplained (as is the subtle difference between modern seawater Ge/Si and core top radiolarian Ge/Si), but it is interesting to note that an offset in silicon isotope fractionation is also observed between *Spumellaria* and *Nassellaria* (Doering et al., 2021). That fractionation has been interpreted (Doering et al, 2021) as reflecting differences in Si-uptake pathways between the orders of Radiolaria (as have been observed for diatoms, e.g., Sutton et al., 2013). It is unclear how or if differences in silicification pathways would affect Ge/Si discrimination across radiolarian taxa, but there is no reason to suspect that such processes would change during the few hundred kyr of the MECO.

At the start of the MECO, as defined by the warming trend in benthic $\delta^{18}O$, spumellarian Ge/Si values average ~0.46 μmol/mol with a slightly negative trend down to ~0.41 at 40.3 Ma while nassellarian Ge/Si averages ~0.34 μmol/mol with minimal

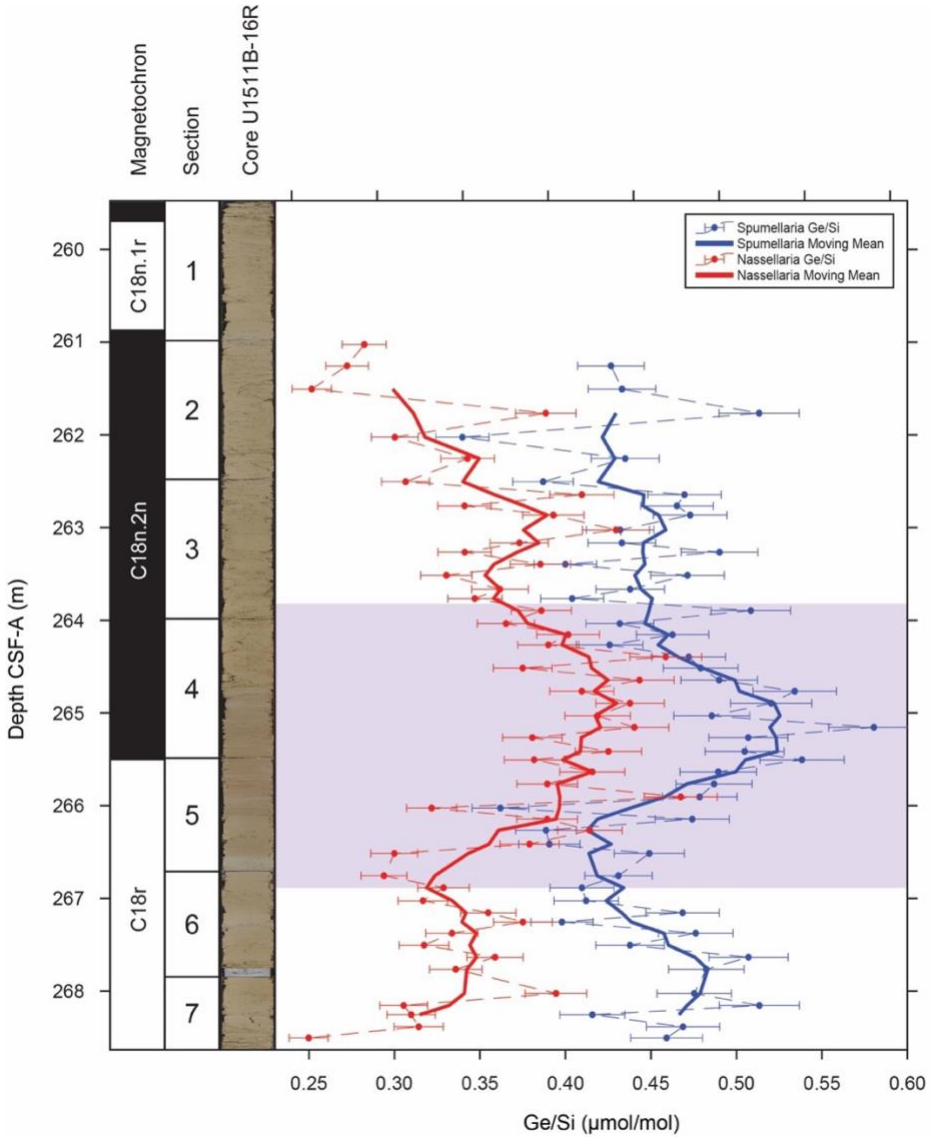

Figure 10. Ge/Si versus depth for Core 371-U1511B-16R. Core image, section divisions, magnetochrons (Dallanave and Chang, 2020), and depth are shown. Ge/Si values are separated by morphospecies. Red denotes nassellarian data while blue represents spumellarian data. Ge/Si values are shown by colored circles connected by dashed lines. The solid lines represent the 5-point moving means for both datasets. Error bars reflect long-term external precision of a consistency standard (= 0.0457, 1 s.d.). The purple shaded region indicates the peak-MECO interval as defined by correlation to peak-warming indicated by benthic foraminiferal $\delta^{18}O$ data from ODP Site 738 (Figure 11). Ge/Si values for both morphospecies range from ~0.25 to 0.55 µmol/mol (similar to modern radiolarian Ge/Si). Both morphospecies display similar trends, though spumellarian samples consistently return Ge/Si values that are 30% higher than nassellarian samples. There is a 20-25% increase in Ge/Si values just before the base of Chron C18.2n in both morphospecies records.

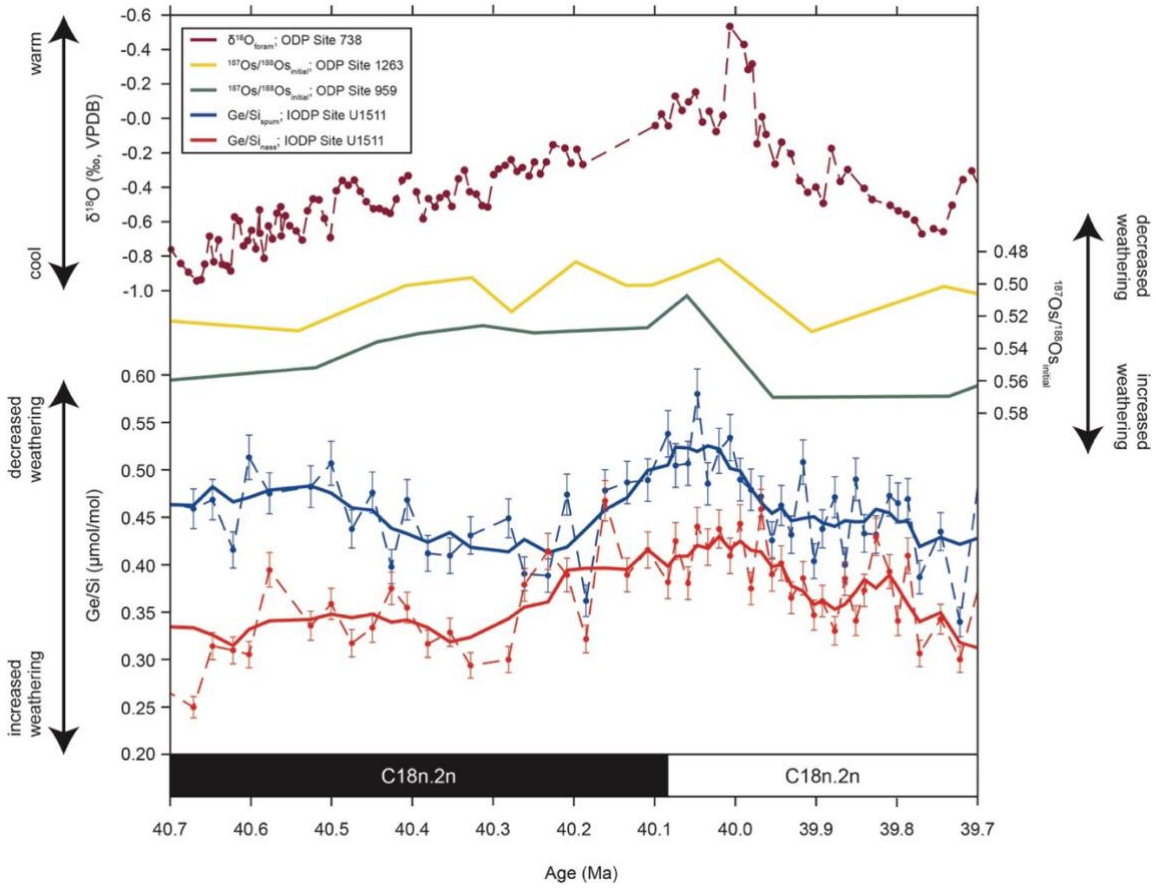

Figure 11. Comparison of new Ge/Si records to benthic foraminiferal $\delta^{18}O$ from ODP Site 738 (Bohaty et al., 2009) and two $^{187}Os/^{188}Os$ records from ODP sites 1263 and 959 (van der Ploeg et al., 2018). Ages were determined using an age model developed by Bohaty et al. (2009). The Ge/Si and $^{187}Os/^{188}Os$ records appear to correlate with each other and reach peak values around the same time. In contrast, while the Ge/Si and $\delta^{18}O$ records have similar trends, the peak Ge/Si values precede peak $\delta^{18}O$ values by tens of thousands of years. For this comparison $\delta^{18}O$ values indicate temperature changes while Ge/Si and $^{187}Os/^{188}Os$ generally indicate changes to the weathering flux.

change until 40.3 Ma (Figure 10). Starting at 40.3 Ma, both records show rises in Ge/Si until reaching peak values (Spumellaria = average ~0.51 μmol/mol; Nassellaria = average ~0.42 μmol/mol) just before 40.1 Ma, representing a 20-25% increase in Ge/Si ratio in both records (Figure 10). After the MECO peak, Ge/Si ratios in both orders decline relatively rapidly (by 39.95 Ma) to values close to those preceding the peak-MECO (Figure 10).

When compared to a record of benthic foraminiferal $\delta^{18}O$ from ODP Site 738 and two $^{187}Os/^{188}Os$ records from ODP sites 1263 and 959, Ge/Si values appear to follow similar, but not completely correlative trends (Figure 11; Bohaty et al., 2009; van der Ploeg et al., 2018). The increase in Ge/Si generally correlates with the period of declining benthic $\delta^{18}O$ (warming), and the Ge/Si decrease corresponds with the post-MECO cooling. However, perhaps the most notable difference is the slight lag of minimum $\delta^{18}O$ values following peak Ge/Si. The highest Ge/Si values for both orders precede $\delta^{18}O$ minima by tens of thousands of years (Figure 11). The Ge/Si and $^{187}Os/^{188}Os$ record, in contrast, both peak around the same time and are in general agreement with each other (Figure 11).

DISCUSSION

Ge/Si Interpretations

To determine why the MECO differs from Paleogene hyperthermals, I used the Ge/Si of radiolarians from IODP Site U1511 to investigate the behavior of silicate weathering across the MECO. Ge/Si records have previously been interpreted to represent either a change in the relative strength of the input fluxes or a change in the

removal of the dissolved ions from seawater. While I favor the former hypothesis and its implications for continental silicate weathering, the alternative hypothesis is considered below.

Reverse Weathering-Controlled Ge/Si

The sink-controlled hypothesis proposes that shifts in seawater Ge/Si depend not on the relative strengths of the primary inputs, but instead on the proportion of Ge sequestered by authigenic mineral formation in primarily marginal marine environments via reverse weathering (Hammond et al., 2000; King et al., 2000; McManus et al., 2003; Hammond et al., 2004). Previous authors suggested water column temperature as a potential mechanism to control the relative strength of this sink (Hammond et al., 2004).

This would result in Ge/Si values disconnected from the weathering flux. This might account for the variable opal mass accumulation observed across the MECO (e.g., Witkowski et al., 2014). The abundance of biogenic opal observed in the sediment record may be an indicator of increased weathering flux to the ocean as a response to increased Si delivery (Penman, 2016; Penman et al., 2019). However, regional opal burial is also strongly linked with circulation (e.g., Akagi and Nishino, 2021) and while some regions do show increased burial (Witkowski et al., 2012; Witkowski et al., 2014), there appears to be a geographically variable response of primary productivity across the MECO (Witkowski et al., 2014). Therefore, opal burial may not be a strong indicator of continental weathering changes.

Despite model results from Hammond et al. (2004) showing the potential to account for changes in Ge/Si over glacial-interglacial periods and in the Miocene by

temperature alone, the absence of identified Ge-incorporating authigenic minerals in marginal settings, the lack of covariance of Ge/Si with temperature in other studies, and the agreement of Ge/Si with established weathering proxies supports the hypothesis that continental weathering is the predominant control on changing Ge/Si in our record. Despite Ge depletion being identified in marine porewater profiles, there has yet to be a mineral phase implicated in incorporating the Ge and removing it from the ocean reservoir (Baronas, 2017). Furthermore, a more recent investigation into the Si cycle demonstrated that the dissolution of biosiliceous material occurs predominantly at the sediment-water interface rather than while sinking through the water column (Tréguer and De La Rocha, 2013). This would suggest that temperature changes in the water column would have minimal effect on the proportion of siliceous particles that reach the seafloor to drive the formation of potential authigenic Ge-enriched phases (Li, 2019). In addition, Ge/Si records from IODP Site U1337 spanning the Mid Miocene Climatic Optimum (MMCO) show little to no change in Ge/Si values across the MMCO or from the Miocene to today, despite recorded warming during this interval and cooling since the Miocene (Li, 2019).

Finally, the Ge/Si record we produced for the MECO appears to be in agreement with the $^{187}Os/^{188}Os$ MECO record while being offset from the $\delta^{18}O$ MECO record, showing that Ge/Si follows a known paleoweathering proxy better than a temperature proxy (Figure 11; Bohaty et al., 2009; van der Ploeg et al., 2018). The peak in $\delta^{18}O$-based temperature follows the peak in Ge/Si after a lag on the order of tens of thousands of years (Figure 11), consistent with changes in silicate weathering (as recorded by Ge/Si) driving a CO_2/climate response.

The above evidence suggests that Ge/Si values are not temperature dependent; however, this does not mean that reverse weathering has no influence on seawater Ge/Si. Instead, at this time we can only refute the proposed mechanism to control the strength of reverse weathering. Further research is needed to discern the process of Ge incorporation during authigenic clay formation in the marine realm, specifically to identify the existence of Ge-incorporating minerals and the controls on the rate of Ge consumption by authigenic clay formation.

Silicate Weathering-Controlled Ge/Si

As the role of reverse weathering on the Ge and Si cycle remains ambiguous, this study will explore the implications of Ge/Si values being controlled primarily by changes in continental silicate weathering. My record displays increasing Ge/Si values leading up to the peak-MECO (Figure 10). Under the assumption that Ge/Si values respond to changes in the flux of continental weathering-derived dissolved silica, we can interpret these findings in one of two ways. First, the overall contribution of continentally sourced, low Ge/Si dissolved silica to the oceans could be reduced due lower silicate weathering rates during the MECO. Second, the Ge/Si of dissolved silica released by silicate weathering could have increased during the MECO.

To achieve the lower rate of silicate weathering required to increase seawater Ge/Si even as temperature and atmospheric CO_2 levels rose during the MECO (Bohaty et al., 2009; Bijl et al., 2010; Henehan et al., 2020), the weatherability of the continents must have been reduced. Weatherability refers to changes in the weathering flux at a given atmospheric CO_2 concentration (Winnick and Maher, 2018; Penman et al., 2020).

The susceptibility of the continents to weathering can change at various spatial and temporal scales. Different regions of Earth's surface chemically weather at different rates depending on the region's temperature, rainfall, atmospheric CO_2 levels, underlying lithology, vegetation, ice cover, and topography (e.g., Kump et al., 2000; West et al., 2005; Penman et al., 2020). The summation of all these regional factors determines global weatherability. Over time, global changes in the aforementioned parameters can influence how weatherable the Earth is. For example, it has been argued that over the past 16 million years the global weatherability increased such that a nearly invariant weathering flux could be sustained at a lower pCO_2, which potentially strengthened the weathering feedback, buffering the climate system from carbon perturbations (Caves et al., 2019). During the Eocene, however, the weathering feedback was generally thought to be weaker (Caves et al., 2016). A transient decrease in global weatherability during the MECO could have resulted in a temporarily lower silicate weathering flux (Figure 12). This would create a carbon-cycle imbalance, with the sources of CO_2 to the atmosphere (mainly volcanic degassing) outweighing the silicate weathering sink. This would drive an increase in pCO_2 before stabilizing at the (higher) pCO_2 required to generate enough weathering to balance the input flux (Figure 12). I argue that just such a transient decrease in the silicate weathering flux produced the observed increase in Ge/Si across the MECO.

To discern whether a reduced continental silicate weathering flux to the oceans could produce the observed shifts in Ge/Si, I performed experiments in a two-box geochemical forward model to investigate the sensitivity of surface ocean Si and Ge concentrations to changes in the flux. The model simplifies the fluxes of Si and Ge into

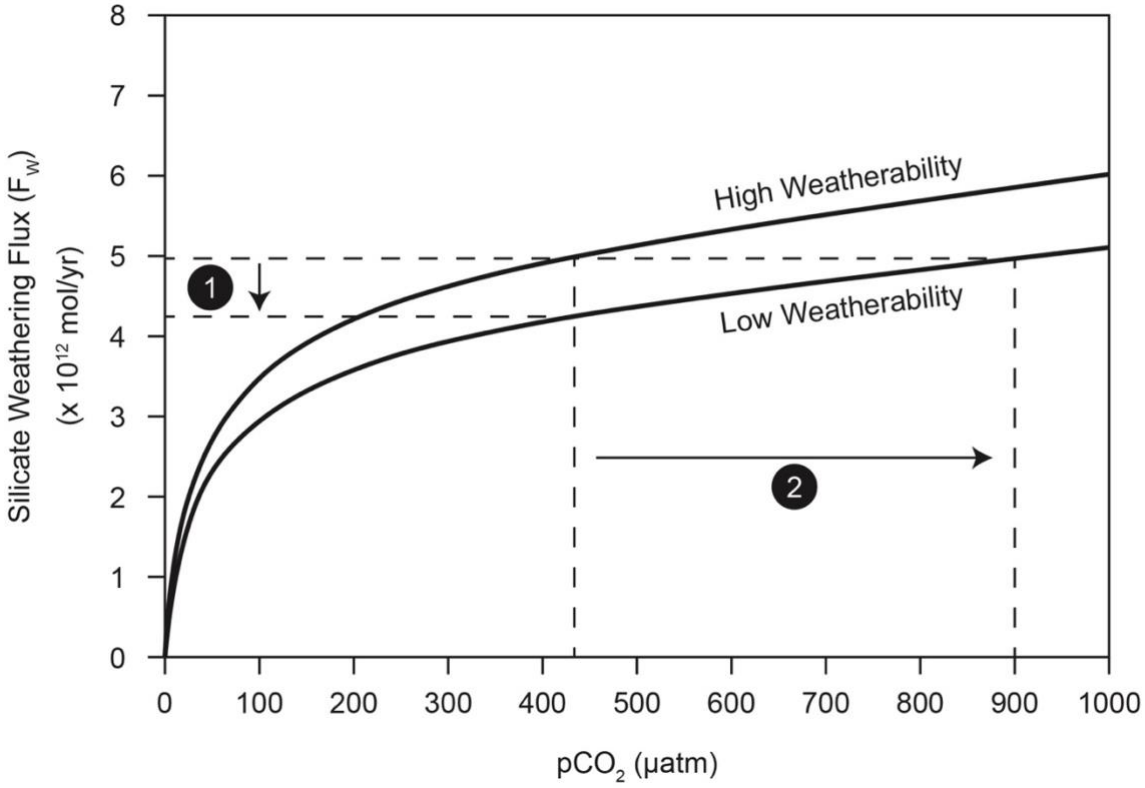

Figure 12. Schematic representation of what a decrease in global weatherability would do to the weathering flux and global pCO_2. If global weatherability were to abruptly decrease without allowing the internal processes of the climate system to keep up, the weathering flux would initially decrease to compensate for the change until pCO_2 levels could rise to return the weathering flux to its initial state. Adapted from Penman et al. (2020).

two inputs, continental and hydrothermal fluids, and two removal mechanisms, opal burial and reverse weathering. After achieving a steady state with known modern parameters (Table 1), changes in the continental input flux were simulated (Figure 13). The model returns Si and Ge concentrations of the surface ocean (upper 100 m).

Multiple scenarios were designed to discern the sensitivity of seawater Ge/Si with variations in the input fluxes (Figure 13). The scenarios that return the most compatible curves with the Site U1511 Ge/Si record are those with a gradual reduction of the continental weathering flux to 40% to 60% of its initial flux over either 200,000 or 400,000 years followed by a return to the baseline input values over 200,000 years (Figure 13). These results show that the observed changes in Ge/Si across the MECO can be accounted for solely by lowering the flux from the continents.

There is, however, another possible influence. Rather than, or in addition to, a change in the weathering flux, the ratio of Ge to Si delivered to the oceans by continental weathering could change, resulting in rising Ge/Si values. Today, different regions of the Earth weather in different ways and can be broadly categorized as either transport-limited or weathering-limited. The former regions are areas in which the rate of weathering reactions outstrip the rate of removal, resulting in the formation of thick cation-depleted soils, while the latter regions supply fresh rock material fast enough that the chemical reactions are not limited by erosion (West et al., 2005).

Today, the global average river Ge/Si concentration (~0.6 μmol/mol) more closely resembles the Ge/Si of weathering-limited regions such as Andean river systems (~0.42 μmol/mol) than that of transport-limited regions like the Amazon basin (~1.7 μmol/mol) (Kump et al., 2000). A global shift in weathering regime from more weathering-limited to

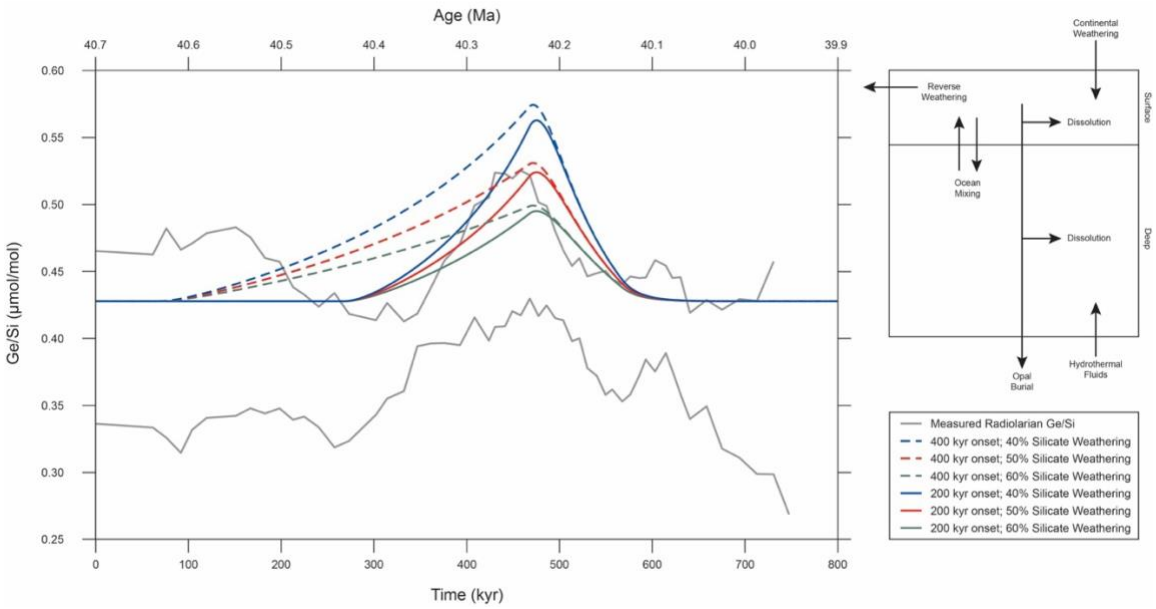

Figure 13. Model simulations of the response of Ge/Si to changes in the continental silicate weathering flux. Six colored scenarios of a gradually decreasing weathering flux over different time periods and to different extents are shown compared to the gray observed Ge/Si moving means. The model scenarios are plotted on the same timescale as the observed data (800 kyr). The scenario specifics are shown in the bottom right. The model schematic is shown in the upper right. The scenario that best fits the observed data is a gradual, linear decrease in silicate weathering to 50% of its original strength over 400 or 200 thousand years with a recovery period of 200 thousand years.

more transport-limited could drive an increase in riverine Ge/Si and thus an increase in seawater Ge/Si. Leading up to the MECO, however, elevated atmospheric CO_2 (Anagnostou et al., 2016) combined with some of the warmest climates of the Cenozoic (Zachos et al., 2008) and generally flat topography led to a chemical weathering intensity that likely exceeded the rates of physical weathering and erosion (Froelich and Misra, 2014). Global weathering was thus likely already much more transport-limited, which makes it difficult to imagine a process or event capable of driving a shift towards even more transport-limited conditions that would result in an increase in seawater Ge/Si.

Furthermore, this explanation does not explain the agreement between my Ge/Si record and the previously published $^{187}Os/^{188}Os$ record. As mentioned above, the observed decrease in $^{187}Os/^{188}Os$ across the MECO implies either an overall decrease in the weathering flux or an increase in the weathering of mantle-derived rocks if we assume hydrothermal activity remains constant on these timescales. Mortlock and Froelich (1987) showed that river Ge/Si, the largest contributor of continental Ge and Si to seawater, does not trend with the mineralogy of its drainage basin. Therefore, the agreement between these two proxies implies that a decrease in the weathering flux did occur across the MECO.

Silicate Weathering as a Driver of Climate

The decrease in silicate weathering rates during the MECO implied by the observed increase in Ge/Si is counterintuitive to how the silicate weathering feedback has been thought to operate during periods of elevated temperature and pCO_2. The assumption that silicate weathering would increase during these periods, however, hinges

on silicate weathering acting as a response to changes in climate. I propose that during the MECO a decrease in silicate weathering instead acted as the driver for warming.

Changes in silicate weathering rates and global weatherability have long been considered a driver of climate on longer timescales, such as for Cenozoic cooling (e.g., Raymo and Ruddiman, 1992; Caves et al., 2016; Caves et al 2019, Jagoutz et al., 2016), the Late Paleozoic Ice Age (LPIA) (e.g., Richey et al., 2020), end-Devonian cooling (e.g., Maffre et al., 2022), and in general throughout the Phanerozoic (Macdonald et al., 2019). Interestingly, these studies all focus on how increased weathering can be a driver for cooling, but the opposite (warming driven by diminished weatherability) must be possible as well. If tectonic uplift (Raymo and Ruddiman, 1992), the emplacement of easily weathered mafic rocks at the surface (Jagoutz et al 2016), and tropical arc-continent collision (Macdonald et al., 2019) are all capable drivers of increased weatherability and global cooling, then the inhibition or cessation of any of those processes can also drive decreased weatherability and global warming.

Diminished silicate weathering acting as a forcing for the MECO could help explain the characteristics that sets the event apart from Paleogene hyperthermals. Instead of an initial large release of carbon driving rapid pCO_2 rise and warming, as in a hyperthermal, a weathering flux decrease would allow for a gradual buildup of pCO_2, consistent with the observed prolonged warming and lack of CIE during the MECO. Furthermore, under decreased silicate weathering rates, the supply of alkalinity to the oceans would decrease, lowering carbonate mineral saturation state (shoaling the CCD) and inhibiting carbonate burial for the duration of the event. Diminished silicate weathering response would also explain why no carbonate overshoot occurred following

the MECO. Without an increased weathering response due to warming, like during a hyperthermal, no overcompensation leading to an over-deepening of the CCD would occur.

CONCLUSIONS

To elucidate why the MECO features several defining characteristics that separate the event from Paleogene hyperthermals, a robust investigation into the behavior of silicate weathering across the MECO is needed. The prolonged, gradual warming, lack of CIE, and persistent absence of carbonate preservation each indicate some failure of the silicate weathering feedback to regulate the climate system as expected. Here I show the viability of using the Ge/Si of siliceous microfossils as a recorder of past weathering flux changes and that during the MECO Ge/Si values indicate that the silicate weathering flux diminished despite that expectation for silicate weathering to increase during periods of elevated temperature and atmospheric CO_2. Moreover, I propose that rather than a feedback, the lowered weathering flux actually acted as the driver of the anomalous features of the MECO. Lowered weathering would result in the gradual warming observed, negating the need for a carbon perturbation, and associated isotope excursion, to initially disturb the climate system, and would also explain how the deepened CCD persisted without producing a carbonate overshoot. This explanation further differentiates the MECO from Paleogene hyperthermals, as the warming event occurred due to an entirely different climate forcing, prompting its unusual characteristics. This places the MECO into a category of its own apart from hyperthermals. In addition, it would redefine the role of silicate weathering on shorter, sub-million-year timescales.

FUTURE WORK

Further study into the mechanism driving variability in Ge/Si records, the indicated diminished weathering flux, and the potential of silicate weathering to act as a driver for warming for the MECO is needed.

Despite agreement with other silicate weathering proxies for the MECO (e.g., van der Ploeg et al., 2018), the Ge/Si system is still largely unconstrained. To determine the environmental controls on Ge and Si uptake in radiolarians I suggest a combination of culturing experiments to observe how Ge is incorporated into the plankton tests and core top analysis to investigate how Ge/Si varies with different regional climates. In addition, a better understanding of the fluxes of Ge and Si to and from the oceans, especially the relative contribution of reverse weathering on whole ocean Ge/Si, is needed.

Further work into the behavior of silicate weathering leading up to, during, and following the MECO is needed. High resolution Ge/Si records from sites around the world would be useful for eliminating the potential of regional influences. The combination of these records with other silicate weathering proxies would shed light on the role of the process in the climate system. These weathering records should also be extended to other geological periods, such as other periods of dramatic climatic change as well as periods of climate stability. These time periods should be reevaluated with the lens that silicate weathering might not only respond, but also influence climate on shorter time scales. These efforts may work to redefine the role that silicate weathering plays in the climate system.

REFERENCES CITED

Akagi, T., and Nishino, H., 2021, Unified modeling of contrasting basin-scale dissolved Al distributions using dissolution kinetics of diatom aggregates: Implication for upwelling intensity as a primary factor to control opal burial rate: Marine Chemistry, v. 235, p. 104009, doi:10.1016/j.marchem.2021.104009.

Anagnostou, E., John, E.H., Edgar, K.M., Foster, G.L., Ridgwell, A., Inglis, G.N., Pancost, R.D., Lunt, D.J., and Pearson, P.N., 2016, Changing atmospheric CO2 concentration was the primary driver of early Cenozoic climate: Nature, v. 533, p. 380–384, doi:10.1038/nature17423.

Azam, F., 1974, Silicic-acid uptake in diatoms studied with [^{68}Ge]germanic acid as tracer: Planta, v. 121, p. 205–212, doi:10.1007/BF00389321.

Babila, T.L., Penman, D.E., Hönisch, B., Kelly, D.C., Bralower, T.J., Rosenthal, Y., and Zachos, J.C., 2018, Capturing the global signature of surface ocean acidification during the Palaeocene–Eocene Thermal Maximum: Philosophical Transactions of the Royal Society A: Mathematical, Physical and Engineering Sciences, v. 376, p. 20170072, doi:10.1098/rsta.2017.0072.

Babila, T.L., Rosenthal, Y., Wright, J.D., and Miller, K.G., 2016, A continental shelf perspective of ocean acidification and temperature evolution during the Paleocene-Eocene Thermal Maximum: Geology, v. 44, p. 275–278, doi:10.1130/G37522.1.

Bareille, G., Labracherie, M., Mortlock, R.A., Maier-Reimer, E., and Froelich, P.N., 1998, A test of $(Ge/Si)_{opal}$ as a paleorecorder of $(Ge/Si)_{seawater}$: Geology, v. 26, p. 179, doi:10.1130/0091-7613(1998)026<0179:ATOGSO>2.3.CO;2.

Barker, S., Greaves, M., and Elderfield, H., 2003, A study of cleaning procedures used for foraminiferal Mg/Ca paleothermometry: Geochemistry, Geophysics, Geosystems, v. 4, p. n/a-n/a, doi:10.1029/2003GC000559.

Baronas, J.J. Germanium and Silicon Isotope Geochemistry in Terrestrial and Marine Low-Temperature Environments [Ph.D.]: University of Southern California, 306 p., https://www.proquest.com/docview/2112741227/abstract/63863AFFFAC4471APQ/1 (accessed July 2023).

Baronas, J.J., Hammond, D.E., Berelson, W.M., McManus, J., and Severmann, S., 2016, Germanium–silicon fractionation in a river-influenced continental margin: The Northern Gulf of Mexico: Geochimica et Cosmochimica Acta, v. 178, p. 124–142, doi:10.1016/j.gca.2016.01.028.

Bijl, P.K., Houben, A.J.P., Schouten, S., Bohaty, S.M., Sluijs, A., Reichart, G.-J., Sinninghe Damsté, J.S., and Brinkhuis, H., 2010, Transient Middle Eocene Atmospheric CO_2 and Temperature Variations: Science, v. 330, p. 819–821, doi:10.1126/science.1193654.

Bohaty, S.M., and Zachos, J.C., 2003, Significant Southern Ocean warming event in the late middle Eocene: Geology, v. 31, p. 1017, doi:10.1130/G19800.1.

Bohaty, S.M., Zachos, J.C., Florindo, F., and Delaney, M.L., 2009, Coupled greenhouse warming and deep-sea acidification in the middle Eocene: Paleoceanography, v. 24, p. n/a-n/a, doi:10.1029/2008PA001676.

Caves, J.K., Jost, A.B., Lau, K.V., and Maher, K., 2016, Cenozoic carbon cycle imbalances and a variable weathering feedback: Earth and Planetary Science Letters, v. 450, p. 152–163, doi:10.1016/j.epsl.2016.06.035.

Caves Rugenstein, J.K., Ibarra, D.E., and Von Blanckenburg, F., 2019, Neogene cooling driven by land surface reactivity rather than increased weathering fluxes: Nature, v. 571, p. 99–102, doi:10.1038/s41586-019-1332-y.

Cohen, A.S., Coe, A.L., Bartlett, J.M., and Hawkesworth, C.J., 1999, Precise Re–Os ages of organic-rich mudrocks and the Os isotope composition of Jurassic seawater: Earth and Planetary Science Letters, v. 167, p. 159–173, doi:10.1016/S0012-821X(99)00026-6.

Cornaggia, F., Bernardini, S., Giorgioni, M., Silva, G.L.X., Nagy, A.I.M., and Jovane, L., 2020, Abyssal oceanic circulation and acidification during the Middle Eocene Climatic Optimum (MECO): Scientific Reports, v. 10, p. 6674, doi:10.1038/s41598-020-63525-3.

Dallanave, E., and Chang, L., 2020, Early Eocene to early Miocene magnetostratigraphic framework for IODP Expedition 371 (Tasman Frontier Subduction Initiation and Paleogene Climate): Newsletters on Stratigraphy, v. 53, p. 365–387, doi:10.1127/nos/2019/0556.

De Argollo, R., and Schilling, J.-G., 1978, Ge–Si and Ga–Al fractionation in Hawaiian volcanic rocks: Geochimica et Cosmochimica Acta, v. 42, p. 623–630, doi:10.1016/0016-7037(78)90007-8.

De La Rocha, C.L., and Bickle, M.J., 2005, Sensitivity of silicon isotopes to whole-ocean changes in the silica cycle: Marine Geology, v. 217, p. 267–282, doi:10.1016/j.margeo.2004.11.016.

Dickens, G.R., 2009, Early Cenozoic Hyperthermals: The Sedimentary Record of Rapid Global Warming and Massive Carbon Input: CSEG Recorder, p. 28–32.

Dickens, G.R., Castillo, M.M., and Walker, J.C.G., 1997, A blast of gas in the latest Paleocene: Simulating first-order effects of massive dissociation of oceanic methane hydrate: Geology, v. 25, p. 259, doi:10.1130/0091-7613(1997)025<0259:ABOGIT>2.3.CO;2.

Doering, K., Ehlert, C., Pahnke, K., Frank, M., Schneider, R., and Grasse, P., 2021, Silicon Isotope Signatures of Radiolaria Reveal Taxon-Specific Differences in Isotope Fractionation: Frontiers in Marine Science, v. 8, p. 666896, doi:10.3389/fmars.2021.666896.

Dunkley-Jones, T., Lunt, D.J., Schmidt, D.N., Ridgwell, A., Sluijs, A., Valdes, P.J., and Maslin, M., 2013, Climate model and proxy data constraints on ocean warming across the Paleocene–Eocene Thermal Maximum: Earth-Science Reviews, v. 125, p. 123–145, doi:10.1016/j.earscirev.2013.07.004.

Elderfield, H., and Schultz, A., 1996, Mid-Ocean Ridge Hydrothermal Fluxes and the Chemical Composition of the Ocean: Annual Review of Earth and Planetary Sciences, v. 24, p. 191–224, doi:10.1146/annurev.earth.24.1.191.

Ellwood, M.J., Kelly, M., Maher, W.A., and De Deckker, P., 2006, Germanium incorporation into sponge spicules: Development of a proxy for reconstructing

inorganic germanium and silicon concentrations in seawater: Earth and Planetary Science Letters, v. 243, p. 749–759, doi:10.1016/j.epsl.2006.01.016.

Ellwood, M.J., and Maher, W.A., 2003, Germanium cycling in the waters across a frontal zone: the Chatham Rise, New Zealand: Marine Chemistry, v. 80, p. 145–159, doi:10.1016/S0304-4203(02)00115-9.

Fontorbe, G., Frings, P.J., De La Rocha, C.L., Hendry, K.R., and Conley, D.J., 2020, Constraints on Earth System Functioning at the Paleocene-Eocene Thermal Maximum From the Marine Silicon Cycle: Paleoceanography and Paleoclimatology, v. 35, doi:10.1029/2020PA003873.

Froelich, P.N., and Andreae, M.O., 1981, The Marine Geochemistry of Germanium: Ekasilicon: Science, v. 213, p. 205–207, doi:10.1126/science.213.4504.205.

Froelich, P.N., Blanc, V., Mortlock, R.A., Chillrud, S.N., Dunstan, W., Udomkit, A., and Peng, T.-H., 1992, River Fluxes of Dissolved Silica to the Ocean Were Higher during Glacials: Ge/Si In Diatoms, Rivers, and Oceans: Paleoceanography, v. 7, p. 739–767, doi:10.1029/92PA02090.

Froelich, P.N., Hambrick, G.A., Andreae, M.O., Mortlock, R.A., and Edmond, J.M., 1985, The geochemistry of inorganic germanium in natural waters: Journal of Geophysical Research, v. 90, p. 1133, doi:10.1029/JC090iC01p01133.

Froelich, F., and Misra, S., 2014, Was the Late Paleocene-Early Eocene Hot Because Earth Was Flat?: An Ocean Lithium Isotope View of Mountain Building, Continental Weathering, Carbon Dioxide, and Earth's Cenozoic Climate: Oceanography, v. 27, p. 36–49.

Garrels, R.M., Lerman, A., and Mackenzie, F.T., 1976, Controls of Atmospheric O 2 and CO 2 : Past, Present, and Future: Geochemical models of the earth's surface environment, focusing on O 2 and CO 2 cycles, suggest that a dynamic steady-state system exists, maintained over time by effective feedback mechanisms: American Scientist, v. 64, p. 306–315.

Gibbs, S.J., Stoll, H.M., Bown, P.R., and Bralower, T.J., 2010, Ocean acidification and surface water carbonate production across the Paleocene–Eocene thermal maximum: Earth and Planetary Science Letters, v. 295, p. 583–592, doi:10.1016/j.epsl.2010.04.044.

Gingerich, P.D., 1989, New earliest Wasatchian mammalian fauna from the Eocene of northwestern Wyoming: composition and diversity in a rarely sampled high-floodplain assemblage: University of Michigan Papers on Paleontology, v. 28, p. 1-97.

Gingerich, P.D., 2001, Paleocene-Eocene Stratigraphy and Biotic Change in the Bighorn and Clarks Fork Basins, Wyoming: University of Michigan Papers on Paleontology, v. 33, p. 1-198.

Hammond, D.E., McManus, J., and Berelson, W.M., 2004, Oceanic germanium/silicon ratios: Evaluation of the potential overprint of temperature on weathering signals: Paleoceanography, v. 19, p. n/a-n/a, doi:10.1029/2003PA000940.

Hammond, D.E., McManus, J., Berelson, W.M., Meredith, C., Klinkhammer, G.P., and Coale, K.H., 2000, Diagenetic fractionation of Ge and Si in reducing sediments: the missing Ge sink and a possible mechanism to cause glacial/interglacial

variations in oceanic Ge/Si: Geochimica et Cosmochimica Acta, v. 64, p. 2453–2465, doi:10.1016/S0016-7037(00)00362-8.

Henehan, M.J., Edgar, K.M., Foster, G.L., Penman, D.E., Hull, P.M., Greenop, R., Anagnostou, E., and Pearson, P.N., 2020, Revisiting the Middle Eocene Climatic Optimum “Carbon Cycle Conundrum” With New Estimates of Atmospheric pCO 2 From Boron Isotopes: Paleoceanography and Paleoclimatology, v. 35, doi:10.1029/2019PA003713.

Intergovernmental Panel on Climate Change (IPCC), 2023, Climate Change 2021 – The Physical Science Basis: Working Group I Contribution to the Sixth Assessment Report of the Intergovernmental Panel on Climate Change: Cambridge, Cambridge University Press, doi:10.1017/9781009157896.

Intergovernmental Panel on Climate Change (IPCC) (Ed.), 2022, Framing and Context, in Global Warming of 1.5°C: IPCC Special Report on Impacts of Global Warming of 1.5°C above Pre-industrial Levels in Context of Strengthening Response to Climate Change, Sustainable Development, and Efforts to Eradicate Poverty, Cambridge, Cambridge University Press, p. 49–92, doi:10.1017/9781009157940.003.

Jagoutz, O., Macdonald, F.A., and Royden, L., 2016, Low-latitude arc–continent collision as a driver for global cooling: Proceedings of the National Academy of Sciences, v. 113, p. 4935–4940, doi:10.1073/pnas.1523667113.

Kelly, D.C., Nielsen, T.M.J., and Schellenberg, S.A., 2012, Carbonate saturation dynamics during the Paleocene–Eocene thermal maximum: Bathyal constraints

from ODP sites 689 and 690 in the Weddell Sea (South Atlantic): Marine Geology, v. 303–306, p. 75–86, doi:10.1016/j.margeo.2012.02.003.

Kelly, D.C., Zachos, J.C., Bralower, T.J., and Schellenberg, S.A., 2005, Enhanced terrestrial weathering/runoff and surface ocean carbonate production during the recovery stages of the Paleocene-Eocene thermal maximum: Paleoceanography, v. 20, p. n/a-n/a, doi:10.1029/2005PA001163.

Kennett, J.P., and Stott, L.D., 1991, Abrupt deep-sea warming, palaeoceanographic changes and benthic extinctions at the end of the Palaeocene: Nature, v. 353, p. 225–229, doi:10.1038/353225a0.

King, S.L., Froelich, P.N., and Jahnke, R.A., 2000, Early diagenesis of germanium in sediments of the Antarctic South Atlantic: in search of the missing Ge sink: Geochimica et Cosmochimica Acta, v. 64, p. 1375–1390, doi:10.1016/S0016-7037(99)00406-8.

Kirtland Turner, S., Hull, P.M., Kump, L.R., and Ridgwell, A., 2017, A probabilistic assessment of the rapidity of PETM onset: Nature Communications, v. 8, p. 353, doi:10.1038/s41467-017-00292-2.

Koch, P.L., Zachos, J.C., and Gingerich, P.D., 1992, Correlation between isotope records in marine and continental carbon reservoirs near the Palaeocene/Eocene boundary: Nature, v. 358, p. 319–322, doi:10.1038/358319a0.

Kump, L.R., Brantley, S.L., and Arthur, M.A., 2000, Chemical Weathering, Atmospheric CO_2, and Climate: Annual Review of Earth and Planetary Sciences, v. 28, p. 611–667, doi:10.1146/annurev.earth.28.1.611.

Kurtz, A.C., Derry, L.A., and Chadwick, O.A., 2002, Germanium-silicon fractionation in the weathering environment: Geochimica et Cosmochimica Acta, v. 66, p. 1525–1537, doi:10.1016/S0016-7037(01)00869-9.

Lazarus, D., Suzuki, N., Ishitani, Y., and Takahashi, K., 2020, Paleobiology of the Polycystine Radiolaria: John Wiley & Sons, 528 p.

Li, J., 2019, Germanium-silicon Ratios as a Record of Mid Miocene Silica Fluxes to the Oceans [M.S.]: Cornell University, 126 p., https://www.proquest.com/docview/2300629399?pq-origsite=gscholar&fromopenview=true (accessed July 2023).

Lin, H.-L., and Chen, C.-J., 2002, A late Pliocene diatom Ge/Si record from the Southeast Atlantic: Marine Geology, v. 180, p. 151–161, doi:10.1016/S0025-3227(01)00211-0.

Lu, X., Kendall, B., Stein, H.J., and Hannah, J.L., 2017, Temporal record of osmium concentrations and $^{187}Os/^{188}Os$ in organic-rich mudrocks: Implications for the osmium geochemical cycle and the use of osmium as a paleoceanographic tracer: Geochimica et Cosmochimica Acta, v. 216, p. 221–241, doi:10.1016/j.gca.2017.06.046.

Macdonald, F.A., Swanson-Hysell, N.L., Park, Y., Lisiecki, L., and Jagoutz, O., 2019, Arc-continent collisions in the tropics set Earth's climate state: Science, v. 364, p. 181–184, doi:10.1126/science.aav5300.

Maffre, P., Godderis, Y., Pohl, A., Donnadieu, Y., Carretier, S., and Le Hir, G., 2022, The complex response of continental silicate rock weathering to the colonization of

the continents by vascular plants in the Devonian: American Journal of Science, v. 322, p. 461–492, doi:10.2475/03.2022.02.

McInerney, F.A., and Wing, S.L., 2011, The Paleocene-Eocene Thermal Maximum: A Perturbation of Carbon Cycle, Climate, and Biosphere with Implications for the Future: Annual Review of Earth and Planetary Sciences, v. 39, p. 489–516, doi:10.1146/annurev-earth-040610-133431.

McManus, J., Hammond, D.E., Cummins, K., Klinkhammer, G.P., and Berelson, W.M., 2003, Diagenetic Ge-Si fractionation in continental margin environments: further evidence for a nonopal Ge sink: Geochimica et Cosmochimica Acta, v. 67, p. 4545–4557, doi:10.1016/S0016-7037(03)00385-5.

Mortlock, R.A., and Froelich, P.N., 1986, Hydrothermal Germanium Over the Southern East Pacific Rise: Science, v. 231, p. 43–45, doi:10.1126/science.231.4733.43.

Mortlock, R.A., Froelich, P.N., Feely, R.A., Massoth, G.J., Butterfield, D.A., and Lupton, J.E., 1993, Silica and germanium in Pacific Ocean hydrothermal vents and plumes: Earth and Planetary Science Letters, v. 119, p. 365–378, doi:10.1016/0012-821X(93)90144-X.

Mortlock, R.A., and Frohlich, P.N., 1987, Continental weathering of germanium: Ge/Si in the global river discharge: Geochimica et Cosmochimica Acta, v. 51, p. 2075–2082, doi:10.1016/0016-7037(87)90257-2.

Murnane, R.J., Leslie, B., Hammond, D.E., and Stallard, R.F., 1989, Germanium geochemistry in the Southern California Borderlands: Geochimica et Cosmochimica Acta, v. 53, p. 2873–2882, doi:10.1016/0016-7037(89)90164-6.

Nunes, F., and Norris, R.D., 2006, Abrupt reversal in ocean overturning during the Palaeocene/Eocene warm period: Nature, v. 439, p. 60–63, doi:10.1038/nature04386.

Opfergelt, S., Cardinal, D., André, L., Delvigne, C., Bremond, L., and Delvaux, B., 2010, Variations of δ^{30}Si and Ge/Si with weathering and biogenic input in tropical basaltic ash soils under monoculture: Geochimica et Cosmochimica Acta, v. 74, p. 225–240, doi:10.1016/j.gca.2009.09.025.

Pagani, M., Caldeira, K., Archer, D., and Zachos, J.C., 2006, An Ancient Carbon Mystery: Science, v. 314, p. 1556–1557, doi:10.1126/science.1136110.

Panchuk, K., Ridgwell, A., and Kump, L.R., 2008, Sedimentary response to Paleocene-Eocene Thermal Maximum carbon release: A model-data comparison: Geology, v. 36, p. 315–318, doi:10.1130/G24474A.1.

Penman, D.E. et al., 2016, An abyssal carbonate compensation depth overshoot in the aftermath of the Palaeocene–Eocene Thermal Maximum: Nature Geoscience, v. 9, p. 575–580, doi:10.1038/ngeo2757.

Penman, D.E., 2016, Silicate weathering and North Atlantic silica burial during the Paleocene-Eocene Thermal Maximum: Geology, v. 44, p. 731–734, doi:10.1130/G37704.1.

Penman, D.E., Caves Rugenstein, J.K., Ibarra, D.E., and Winnick, M.J., 2020, Silicate weathering as a feedback and forcing in Earth's climate and carbon cycle: Earth-Science Reviews, v. 209, p. 103298, doi:10.1016/j.earscirev.2020.103298.

Penman, D.E., Hönisch, B., Zeebe, R.E., Thomas, E., and Zachos, J.C., 2014, Rapid and sustained surface ocean acidification during the Paleocene-Eocene Thermal Maximum: Paleoceanography, v. 29, p. 357–369, doi:10.1002/2014PA002621.

Penman, D.E., and Rooney, A.D., 2019, Coupled carbon and silica cycle perturbations during the Marinoan snowball Earth deglaciation: Geology, v. 47, p. 317–320, doi:10.1130/G45812.1.

Percival, L.M.E., Cohen, A.S., Davies, M.K., Dickson, A.J., Hesselbo, S.P., Jenkyns, H.C., Leng, M.J., Mather, T.A., Storm, M.S., and Xu, W., 2016, Osmium isotope evidence for two pulses of increased continental weathering linked to Early Jurassic volcanism and climate change: Geology, v. 44, p. 759–762, doi:10.1130/G37997.1.

Peucker-Ehrenbrink, B., and Ravizza, G., 2000, The marine osmium isotope record: Terra Nova, v. 12, p. 205–219, doi:10.1046/j.1365-3121.2000.00295.x.

Qi, H.-W., Hu, R.-Z., Jiang, K., Zhou, T., Liu, Y.-F., and Xiong, Y.-W., 2019, Germanium isotopes and Ge/Si fractionation under extreme tropical weathering of basalts from the Hainan Island, South China: Geochimica et Cosmochimica Acta, v. 253, p. 249–266, doi:10.1016/j.gca.2019.03.022.

Raymo, M.E., and Ruddiman, W.F., 1992, Tectonic forcing of late Cenozoic climate: Nature, v. 359, p. 117–122, doi:10.1038/359117a0.

Richey, J.D., Montañez, I.P., Goddéris, Y., Looy, C.V., Griffis, N.P., and DiMichele, W.A., 2020, Influence of temporally varying weatherability on CO_2–climate coupling and ecosystem change in the late Paleozoic: Greenhouse Gases/Terrestrial Archives/Pre-Cenozoic preprint, doi:10.5194/cp-2020-50.

Rouxel, O., Galy, A., and Elderfield, H., 2006, Germanium isotopic variations in igneous rocks and marine sediments: Geochimica et Cosmochimica Acta, v. 70, p. 3387–3400, doi:10.1016/j.gca.2006.04.025.

Shemesh, A., Mortlock, R.A., and Froelich, P.N., 1989, Late Cenozoic Ge/Si record of marine biogenic opal: Implications for variations of riverine fluxes to the ocean: Paleoceanography, v. 4, p. 221–234, doi:10.1029/PA004i003p00221.

Shemesh, A., Mortlock, R.A., Smith, R.J., and Froelich, P.N., 1988, Determination of Ge/Si in marine siliceous microfossils: Separation, cleaning and dissolution of diatoms and radiolaria: Marine Chemistry, v. 25, p. 305–323, doi:10.1016/0304-4203(88)90113-2.

Sluijs, A., Bijl, P.K., Schouten, S., Röhl, U., Reichart, G.-J., and Brinkhuis, H., 2011, Southern ocean warming, sea level and hydrological change during the Paleocene-Eocene thermal maximum: Climate of the Past, v. 7, p. 47–61, doi:10.5194/cp-7-47-2011.

Sluijs, A., Bowen, G.J., Brinkhuis, H., Lourens, L.J., and Thomas, E., 2007, The Palaeocene–Eocene Thermal Maximum super greenhouse: biotic and geochemical signatures, age models and mechanisms of global change, in Williams, M., Haywood, A.M., Gregory, F.J., and Schmidt, D.N. eds., Deep-Time Perspectives on Climate Change: Marrying the Signal from Computer Models and Biological Proxies, The Geological Society of London on behalf of The Micropalaeontological Society, p. 323–349, doi:10.1144/TMS002.15.

Sluijs, A., Zeebe, R.E., Bijl, P.K., and Bohaty, S.M., 2013, A middle Eocene carbon cycle conundrum: Nature Geoscience, v. 6, p. 429–434, doi:10.1038/ngeo1807.

Sutherland, R., Dickens, G.R., Blum, P., and Expedition 371 Scientists (Eds.), 2019, Tasman Frontier Subduction Initiation and Paleogene Climate: Site U1511: International Ocean Discovery Program, Proceedings of the International Ocean Discovery Program, v. 371, doi:10.14379/iodp.proc.371.2019.

Sutton, J., Ellwood, M.J., Maher, W.A., and Croot, P.L., 2010, Oceanic distribution of inorganic germanium relative to silicon: Germanium discrimination by diatoms: Global Biogeochemical Cycles, v. 24, p. n/a-n/a, doi:10.1029/2009GB003689.

Sutton, J.N., Varela, D.E., Brzezinski, M.A., and Beucher, C.P., 2013, Species-dependent silicon isotope fractionation by marine diatoms: Geochimica et Cosmochimica Acta, v. 104, p. 300–309, doi:10.1016/j.gca.2012.10.057.

Thomas, E., 1998, Biogeography of the Late Paleocene Benthic Foraminiferal Extinction, in Columbia University Press, p. 214–243.

Thomas, E., 2007, Cenozoic mass extinctions in the deep sea: What perturbs the largest habitat on Earth?, in Large Ecosystem Perturbations: Causes and Consequences, Geological Society of America, doi:10.1130/2007.2424(01).

Tipple, B.J., Pagani, M., Krishnan, S., Dirghangi, S.S., Galeotti, S., Agnini, C., Giusberti, L., and Rio, D., 2011, Coupled high-resolution marine and terrestrial records of carbon and hydrologic cycles variations during the Paleocene–Eocene Thermal Maximum (PETM): Earth and Planetary Science Letters, v. 311, p. 82–92, doi:10.1016/j.epsl.2011.08.045.

Tréguer, P.J. et al., 2021, Reviews and syntheses: The biogeochemical cycle of silicon in the modern ocean: Biogeosciences, v. 18, p. 1269–1289, doi:10.5194/bg-18-1269-2021.

Tréguer, P.J., and De La Rocha, C.L., 2013, The World Ocean Silica Cycle: Annual Review of Marine Science, v. 5, p. 477–501, doi:10.1146/annurev-marine-121211-172346.

Tréguer, P., Nelson, D.M., Van Bennekom, A.J., DeMaster, D.J., Leynaert, A., and Quéguiner, B., 1995, The Silica Balance in the World Ocean: A Reestimate: Science, v. 268, p. 375–379, doi:10.1126/science.268.5209.375.

Tripati, A., and Elderfield, H., 2005, Deep-Sea Temperature and Circulation Changes at the Paleocene-Eocene Thermal Maximum: Science, v. 308, p. 1894–1898, doi:10.1126/science.1109202.

van der Ploeg, R., Selby, D., Cramwinckel, M.J., Li, Y., Bohaty, S.M., Middelburg, J.J., and Sluijs, A., 2018, Middle Eocene greenhouse warming facilitated by diminished weathering feedback: Nature Communications, v. 9, p. 2877, doi:10.1038/s41467-018-05104-9.

Walker, J.C.G., Hays, P.B., and Kasting, J.F., 1981, A negative feedback mechanism for the long-term stabilization of Earth's surface temperature: Journal of Geophysical Research, v. 86, p. 9776, doi:10.1029/JC086iC10p09776.

Wang, Y., Zhao, T., Xu, Z., Sun, H., and Zhang, J., 2022, Ge/Si Ratio of River Water in the Yarlung Tsangpo: Implications for Hydrothermal Input and Chemical Weathering: Water, v. 14, p. 181, doi:10.3390/w14020181.

West, A., Galy, A., and Bickle, M., 2005, Tectonic and climatic controls on silicate weathering: Earth and Planetary Science Letters, v. 235, p. 211–228, doi:10.1016/j.epsl.2005.03.020.

Westerhold, T. et al., 2020, An astronomically dated record of Earth's climate and its predictability over the last 66 million years: Science, v. 369, p. 1383–1387, doi:10.1126/science.aba6853.

Wing, S.L., Harrington, G.J., Smith, F.A., Bloch, J.I., Boyer, D.M., and Freeman, K.H., 2005, Transient Floral Change and Rapid Global Warming at the Paleocene-Eocene Boundary: Science, v. 310, p. 993–996, doi:10.1126/science.1116913.

Winnick, M.J., and Maher, K., 2018, Relationships between CO2, thermodynamic limits on silicate weathering, and the strength of the silicate weathering feedback: Earth and Planetary Science Letters, v. 485, p. 111–120, doi:10.1016/j.epsl.2018.01.005.

Witkowski, J., Bohaty, S.M., Edgar, K.M., and Harwood, D.M., 2014, Rapid fluctuations in mid-latitude siliceous plankton production during the Middle Eocene Climatic Optimum (ODP Site 1051, western North Atlantic): Marine Micropaleontology, v. 106, p. 110–129, doi:10.1016/j.marmicro.2014.01.001.

Witkowski, J., Bohaty, S.M., McCartney, K., and Harwood, D.M., 2012, Enhanced siliceous plankton productivity in response to middle Eocene warming at Southern Ocean ODP Sites 748 and 749: Palaeogeography, Palaeoclimatology, Palaeoecology, v. 326–328, p. 78–94, doi:10.1016/j.palaeo.2012.02.006.

Zachos, J.C. et al., 2005, Rapid Acidification of the Ocean During the Paleocene-Eocene Thermal Maximum: Science, v. 308, p. 1611–1615, doi:10.1126/science.1109004.

Zachos, J.C., Dickens, G.R., and Zeebe, R.E., 2008, An early Cenozoic perspective on greenhouse warming and carbon-cycle dynamics: Nature, v. 451, p. 279–283, doi:10.1038/nature06588.

Zachos, J., Pagani, M., Sloan, L., Thomas, E., and Billups, K., 2001, Trends, Rhythms, and Aberrations in Global Climate 65 Ma to Present: Science, v. 292, p. 686–693, doi:10.1126/science.1059412.

Zachos, J.C., Schouten, S., Bohaty, S., Quattlebaum, T., Sluijs, A., Brinkhuis, H., Gibbs, S.J., and Bralower, T.J., 2006, Extreme warming of mid-latitude coastal ocean during the Paleocene-Eocene Thermal Maximum: Inferences from TEX86 and isotope data: Geology, v. 34, p. 737, doi:10.1130/G22522.1.

Zeebe, R.E., Zachos, J.C., and Dickens, G.R., 2009, Carbon dioxide forcing alone insufficient to explain Palaeocene–Eocene Thermal Maximum warming: Nature Geoscience, v. 2, p. 576–580, doi:10.1038/ngeo578.

Appendix

Table A1. Sample depths, assigned ages, and Ge/Si values. Samples were collected from IODP Expedition 371 Site U1511B throughout cores 16 and 17. The middle depth for each sample was used to calculate the corresponding age of the sediments using two age models (Bohaty et al., 2009; Westerhold et al., 2020). The tie points used to construct the age models are shown in Table A2. The Ge/Si values for *Spumellaria* and *Nassellaria* samples were determined using an inductively coupled plasma mass spectrometer (ICP-MS) at Utah State's Core Microscopy Lab.

Sample ID (371-U1511B-)	Top Depth (CSF-A, m)	Bottom Depth (CSF-A, m)	Middle Depth (CSF-A, m)	Age (Ma, Westerhold)	Age (Ma, Bohaty)	Ge/Si (Spum; µmol/mol)	Ge/Si (Nass µmol/mol)
16R-2W-2/3	261.02	261.03	261.03	39.95	39.62		0.28
16R-2W-25/26	261.25	261.26	261.26	39.97	39.64	0.43	0.27
16R-2W-50/51	261.50	261.51	261.51	39.99	39.67	0.43	0.25
16R-2W-76/77	261.76	261.77	261.77	40.01	39.69	0.51	0.39
16R-2W-102/103	262.02	262.03	262.03	40.02	39.72	0.34	0.30
16R-2W-125/126	262.25	262.26	262.26	40.04	39.75	0.43	0.34
16R-3W-0/1	262.50	262.51	262.51	40.06	39.77	0.39	0.31
16R-3W-14/15	262.64	262.65	262.65	40.07	39.79	0.47	0.41
16R-3W-26/27	262.76	262.77	262.77	40.08	39.80	0.47	0.34
16R-3W-36/37	262.86	262.87	262.87	40.09	39.81	0.47	0.39
16R-3W-52/53	263.02	263.03	263.03	40.10	39.83	0.43	0.43
16R-3W-66/67	263.16	263.17	263.17	40.11	39.84	0.43	0.37
16R-3W-76/77	263.26	263.27	263.27	40.11	39.85	0.49	0.34
16R-3W-89/90	263.39	263.40	263.40	40.12	39.86	0.40	0.39
16R-3W-101/102	263.51	263.52	263.52	40.13	39.88	0.47	0.33
16R-3W-116/117	263.66	263.67	263.67	40.14	39.89	0.44	0.36
16R-3W-126/127	263.76	263.77	263.77	40.15	39.90	0.40	0.35
16R-3W-139/140	263.89	263.90	263.90	40.16	39.92	0.51	0.39
16R-4W-3/4	264.03	264.04	264.04	40.17	39.93	0.43	0.37
16R-4W-15/16	264.15	264.16	264.16	40.18	39.94	0.46	0.40
16R-4W-26/27	264.26	264.27	264.27	40.19	39.95	0.43	0.39
16R-4W-39/40	264.39	264.40	264.40	40.20	39.97	0.47	0.46
16R-4W-51/52	264.51	264.52	264.52	40.20	39.98	0.48	0.37
16R-4W-64/65	264.64	264.65	264.65	40.21	39.99	0.49	0.44
16R-4W-76/77	264.76	264.77	264.77	40.22	40.01	0.53	0.41
16R-4W-89/90	264.89	264.90	264.90	40.23	40.02	0.52	0.44
16R-4W-102/104	265.02	265.04	265.03	40.24	40.03	0.49	0.42
16R-4W-115/116	265.15	265.16	265.16	40.25	40.05	0.58	0.44
16R-4W-126/127	265.26	265.27	265.27	40.26	40.06	0.51	0.38
16R-4W-141/142	265.41	265.42	265.42	40.27	40.07	0.50	0.42
16R-5W-0/1	265.50	265.51	265.51	40.28	40.08	0.54	0.38
16R-5W-13/14	265.63	265.64	265.64	40.29	40.11	0.49	0.42
16R-5W-26/27	265.76	265.77	265.77	40.31	40.13	0.49	0.39
16R-5W-40/41	265.90	265.91	265.91	40.32	40.16	0.48	0.47
16R-5W-52/53	266.02	266.03	266.03	40.34	40.18	0.36	0.32
16R-5W-64/65	266.14	266.15	266.15	40.35	40.21	0.47	0.39
16R-5W-76/77	266.26	266.27	266.27	40.37	40.23	0.39	0.41
16R-5W-91/92	266.41	266.42	266.42	40.39	40.26	0.39	0.38
16R-5W-101/102	266.51	266.52	266.52	40.40	40.28	0.45	0.30
16R-6W-3/4	266.75	266.76	266.76	40.43	40.33	0.43	0.29
16R-6W-16/17	266.88	266.89	266.89	40.44	40.35	0.41	0.33

16R-6W-30/31	267.02	267.03	267.03	40.46	40.38	0.41	0.32
16R-6W-43/44	267.15	267.16	267.16	40.48	40.41	0.47	0.35
16R-6W-53/54	267.25	267.26	267.26	40.49	40.43	0.40	0.38
16R-6W-65/66	267.37	267.38	267.38	40.50	40.45	0.48	0.33
16R-6W-78/79	267.50	267.51	267.51	40.52	40.48	0.44	0.32
16R-6W-91/92	267.63	267.64	267.64	40.53	40.50	0.51	0.36
16R-6W-101/102	267.76	267.77	267.77	40.55	40.53	0.48	0.34
16R-7W-16/17	268.02	268.03	268.03	40.58	40.58	0.48	0.39
16R-7W-29/30	268.15	268.16	268.16	40.60	40.60	0.51	0.31
16R-7W-39/40	268.25	268.26	268.26	40.61	40.62	0.42	0.31
16R-7W-52/53	268.38	268.39	268.39	40.62	40.65	0.47	0.31
16R-7W-64/65	268.50	268.51	268.51	40.64	40.67	0.46	0.25
17R-1W-140/141	270.50	270.51	270.51	40.88	41.06	0.55	0.45
17R-2W-141/142	272.02	272.03	272.03	41.06	41.36	0.42	0.34
17R-3W-140/141	273.50	273.51	273.51	41.15	41.43	0.47	0.37
17R-4W-142/143	275.02	275.03	275.03	41.25	41.50	0.53	0.42
17R-6W-133/135	278.02	278.03	278.03	41.48	41.75	0.56	

Table A2. Magnetostratigraphic ages and tie points used for the two age models.

Base of Chron	Middle Depth	Age (Ma, Westerhold)	Age (Ma, Bohaty)
C18n.1r	260.87	39.94	39.60
C18n.2n	265.51	40.28	40.08
C18r	272.01	41.06	41.36
C19n	275.29	41.26	41.51
C19r	287.14	42.20	42.54